UNIVERSITY OF OKLAHOMA GRADUATE COLLEGE

ENHANCING SPECIFIC DIFFERENTIAL PHASE ESTIMATION BY ISOLATING DIFFERENTIAL BACKSCATTERING PHASE TO IMPROVE SEVERE WEATHER DETECTION

A THESIS

SUBMITTED TO THE GRADUATE FACULTY

in partial fulfillment of the requirements for the
Degree of

MASTER OF SCIENCE

By Reese Mishler

Norman, Oklahoma
2025

Downloaded from SHAREOK. Persistent Handle URL: https://hdl.handle.net/11244/341357

ENHANCING SPECIFIC DIFFERENTIAL PHASE ESTIMATION BY ISOLATING DIFFERENTIAL BACKSCATTERING PHASE TO IMPROVE SEVERE WEATHER DETECTION

A THESIS APPROVED FOR THE

SCHOOL OF METEOROLOGY

BY THE COMMITTEE CONSISTING OF

Dr. Guifu Zhang, Chair

Dr. Vivek Mahale

Dr. Feng Xu

© Copyright by REESE MISHLER 2025

All Rights Reserved.

Acknowledgment

I would first like to express my gratitude to the National Science Foundation for supporting this work through grant AGS-2136161. I am especially grateful to my advisor, Dr. Guifu Zhang, for his invaluable mentorship, guidance, and support throughout my graduate studies. His encouragement and insight have been instrumental in shaping my growth as a researcher and critical thinker. I also extend my sincere appreciation to Dr. Vivek Mahale and Dr. Feng Xu for serving on my committee and for their valuable feedback, which has greatly contributed to the completion of this thesis. Lastly, I acknowledge that the research presented in this thesis is largely based on the article published in the *Journal of Applied Meteorology and Climatology* (Mishler et al. 2024).

List of Figures

Figure 1: Slide from WDTD radar application course on hail detection (WDTD 2025). 5
Figure 2: Polarized wave with traces of the horizontal polarization (blue) and vertical polarization (red) propagating toward an oblate sphere representing a droplet with the projection of the two polarization onto their respective cross-sections on the drop. 14
Figure 3: Measured radial profile of differential phase (blue) with estimation of ϕ_{DP} (red) and illustrations of δ and ε contained in the measurement. 21
Figure 4: Scattering calculations using the T-matrix method for dry (black) hail and 20% melted hail with water as background (blue), ice as background, and both as inclusions (green): (a) absolute value of backscattering magnitude as a function of diameter for both horizontal (solid) and vertical (dashed) axis. (b) squared ratio of horizontal and vertical absolute scattering magnitude. (c) backscattering phase for both horizontal and vertical axis. (d) differential backscattering phase (δ_a - δ_b). (e) real parts of forward scattering amplitudes for horizontal and vertical axis. (f) difference in real parts of the forward scattering amplitudes. 26
Figure 5: Same as Figure 4 but with 40% melting. 27
Figure 6: Illustration of radar beam resolution volume and associated ϕ_{DP} profile for a) uniform beam filling of Rayleigh regime scatterers and b) non-uniform distribution of Rayleigh regime scatterers. 33
Figure 7: Illustration of radar beam resolution volumes containing different distributions of non-Rayleigh regime scatterers and an associated ϕ_{DP} profile displaying a uniform spatial feature associated with δ. 34
Figure 8: Illustration of radar beam resolution volumes and associated ϕ_{DP} profiles for a) uniformly distributed Rayleigh regime scatterers and b) non-uniform distribution of Rayleigh and non-Rayleigh regime scatterers for a beam passing through the melting layer. 35
Figure 9: Measured radial profile of differential phase (blue) with LSF estimation of ϕ_{DP} (red line). 37
Figure 10: Low-elevation (0.5^o) surveillance mode raw data from KTLX at 2343 UTC on May 04, 2022 of (top left) reflectivity factor (Z_H), (top right) differential reflectivity (Z_{DR}), (bottom left) total differential phase (ϕ_{DP}), and (bottom right) co-polar correlation coefficient (ρ_{hv}). The shaded ray illustrates the 1D radial analyzed in Figure 11. 38

Figure 11: Illustrates the 1D radial profile of reflectivity (Z_H), ϕ_{DP}, and LSF estimated K_{DP} for the shaded ray in Figure 10. 39
Figure 12: flow diagram illustrating the process used for estimating the differential propagation phase (ϕ_{DP}) and specific differential phase (K_{DP}) at a given elevation of a NEXRAD Level II data file. The range gate loop indicates traversing down range of a given radial while the radial loop indicates looping over radials at all azimuth angles. 43
Figure 13: (a) illustrates how an incorrectly classified Rayleigh scattering estimate (circled) can result in a lower bound that causes a down-radial estimation (boxed in red) to be unrealistically high. (b) depicts the same radial estimation of ϕ_{DP} with the faulty segment removed such that the later segment (boxed in red) would have been estimated with the lower bound provided by the previously estimated, up radial segment (circled in black). 46
Figure 14: (a) illustrates ϕ_{DP} (blue) and the unconnected estimated ϕ_{DP} within the determined Rayleigh scattering regimes (red), (b) illustrates the same with linear interpolation used to connect the Rayleigh scattering regimes providing an estimation of ϕ_{DP} in non-Rayleigh scattering regimes. 49
Figure 15: Low-elevation (0.5°) surveillance mode raw data from KTLX at 2330 UTC. (a) reflectivity factor (Z_H), (b) differential reflectivity (Z_{DR}), (c) co-polar correlation coefficient (ρ_{hv}), (d) total differential phase (ϕ_{DP}), (e) hydrometeor classification, and (f) radial velocity. The primary region of enhanced reflectivity is denoted with the black circle in plots a-c while the second region, farther down radial, is denoted with the black box. 51
Figure 16: Ray plots of polarimetric radar data for the highlighted beam in Figure 15: (a) total differential phase (ϕ_{DP}), (b) copolar correlation coefficient (ρ_{hv}), (c) reflectivity factor (Z_H) with horizontal black line at 50 dBZ, and (d) differential reflectivity (Z_{DR}). The region between the vertical orange dashed lines indicate the first region of enhanced Z_H while the region between the dashed black lines indicates the second region of enhanced Z_H. The yellow highlighted region depicts the region of the first 'bump' in ϕ_{DP}. 53
Figure 17: Estimation results for the image data shown in Figure 15: (a) estimated differential propagation phase ϕ_{DP}, (b) estimated differential backscattering phase δ, (c) LP estimated K_{DP}, and (d) LSF estimated K_{DP} 55

Figure 18: Estimation results for the highlighted ray plots in Figure 17: (a) measured total differential phase (blue) and estimated differential propagation phase (red), (b) estimated differential backscattering phase, (c) LSF estimated K_{DP} (blue) and LP estimated K_{DP} (red). 56
Figure 19: Illustrates primary supercell responsible for reported 3” hail in Amber, Oklahoma corresponding with scans depicted in Figure 15 and Figure 16. (a) reflectivity factor (Z_H), (b) estimated differential backscattering phase δ, (c) LP estimated K_{DP}, and (d) LSF estimated K_{DP}. The black outline is used to emphasize the area of enhanced K_{DP} seen in the LSF processing. The region of the significantly enhanced values, which is commonly referred to as ‘KDP foot,’ is denoted by the region within the purple line. 58
Figure 20: Illustrates low-elevation (0.5^o) surveillance mode data from KTLX at 0035 UTC on April 20^{th}, 2023. (a) reflectivity factor (Z_H), (b) differential reflectivity (Z_{DR}), (c) co-polar correlation coefficient (ρ_{hv}), (d) estimated differential backscattering phase (δ), (e) hydrometeor classification, and (f) radial velocity. The black box emphasizes the region of the TDS. 61
Figure 21: Illustrates low-elevation (0.5^o) surveillance mode data from KDGX at 0106 UTC on March 25^{th}, 2023. (a) reflectivity factor (Z_H), (b) differential reflectivity (Z_{DR}), (c) co-polar correlation coefficient (ρ_{hv}), (d) estimated differential backscattering phase (δ), (e) hydrometeor classification, and (f) radial velocity. The black box emphasizes the region of the TDS. 63
Figure 22: (a-c) display 10 by 10 km views of the Z_{DR}, ρ_{hv}, and δ signatures, respectively, for the Rolling Fork, Mississippi tornado illustrated in Figure 21 (d-f) displays the same for the Cole, Oklahoma tornado illustrated in Figure 20. 64

Abstract

Polarimetric radar variables such as differential phase (ϕ_{DP}) and its range derivative, specific differential phase (K_{DP}), are critical for improving quantitative precipitation estimation (QPE) and microphysics retrieval. However, conventional estimation methods for K_{DP} are limited by measurement errors and artifacts arising from the differential backscattering phase (δ), particularly in regions of non-Rayleigh scattering. The presence of δ can introduce significant biases in ϕ_{DP} measurements, leading to errors in K_{DP} estimates and misinterpretations of polarimetric signatures associated with hail and tornado debris. To address these issues, this study develops and applies a novel processing method that leverages classification techniques and Linear Programming (LP) to simultaneously estimate both K_{DP} and δ, reducing error of bias and standard deviation in K_{DP} estimates. The proposed method is implemented using Level II radar data from the WSR-88D network, specifically focusing on 0.5° plan position indicator (PPI) scans. Three cases are analyzed: a hailstorm with a well-defined positive δ signature and two tornado events exhibiting both positive and negative δ signatures, illustrating the variability introduced by resonance scattering effects. Comparisons between the classification-based LP estimator and the operational least-square-fit (LSF) method demonstrate the ability of the proposed approach to improve K_{DP} estimation and reveal the diagnostic potential of δ for identifying hail and tornado debris. These findings support the use of δ as an additional observational parameter for polarimetric radar-based hazard detection.

Table of Contents

Acknowledgment iv
List of Figures v
Abstract viii
1. Introduction 1
2. Background 7
2.1 Single polarization radar variables 8
2.1.1. Reflectivity 8
2.1.2. Radial Velocity 10
2.1.3. Spectrum Width 11
2.2. Dual-polarization variables 12
2.2.1. Differential Reflectivity 15
2.2.2. Co-Polar Correlation Coefficient 16
2.2.3. Differential Phase 19
2.2.4. Specific Differential Phase 21
2.2.5. Overview of Polarimetric Radar Variables 23
2.2 Simulation of Scattering Properties 23
2.3 Non-Uniform Beam Filling 32
2.4 Complications with Estimating K_{DP} 36
3. Data 40
4. Methods 42
5. Results 49
6. Summary and Conclusion 65
References 67

1. Introduction

Weather radar has long been an indispensable tool in meteorology, providing critical insights into atmospheric phenomena. Radar reflectivity and Doppler velocity measurements have significantly advanced weather observation, hazard detection, precipitation quantification, and forecasting (Doviak and Zrnić 1993; Zhang 2016). In recent decades, the advent of dual-polarization (dual-pol) radar technology has introduced a transformative leap in our ability to characterize and understand weather systems. After years of research and development, the national NEXRAD (WSR-88D) network has been upgraded with dual-polarization capabilities, and other national radar networks have also incorporated multiparameter polarimetric radar data (PRD).

Polarimetric radar enhances the traditional capabilities of weather radar by providing multi-parameter measurements that offer unprecedented quality and information about hydrometeors. Unlike single-polarization radar, which transmits and receives pulses in a single orientation, dual-polarization radar transmits and receives both horizontally and vertically polarized waves. This advancement allows for the derivation of new polarimetric radar variables, including differential reflectivity (Z_{DR}), co-polar cross-correlation coefficient (ρ_{hv}), and differential phase (ϕ_{DP}). These variables provide valuable insights into the size, shape, orientation, and composition of cloud and precipitation particles, leading to improved hydrometeor classification and quantitative precipitation estimation (QPE) (Brandes et al. 2002; Ryzhkov et al. 2005a; Huang et al. 2016).

Among these variables, ϕ_{DP} and its derivative specific differential phase (K_{DP}), have proven to be particularly impactful in advancing precipitation estimation. The use of K_{DP} has significantly improved QPE by offering more accurate precipitation rate measurements, especially in heavy rain scenarios. K_{DP}, which represents the difference between propagation constants (wave numbers) of

the polarizations, has shown to outperform traditional reflectivity (Z_H) in both QPE and microphysical retrievals. K_{DP} is particularly advantageous due to its immunity to radar miscalibration, partial beam blockage, and precipitation attenuation. As it is more directly related to the liquid water content in the atmosphere, K_{DP} exhibits reduced sensitivity to hail contamination and variability in the raindrop size distribution (DSD), making it a more reliable parameter for accurate precipitation estimation and microphysical retrievals compared to traditional reflectivity measurements (Aydin et al. 1995; Zrnić and Ryzhkov 1996; Bringi and Chandrasekar 2001; Ryzhkov et al. 2005a; Wang and Chandrasekar 2010; Giangrande et al. 2013; Huang et al. 2016; Ralph-Hampton 2022).

However, despite its advantages, obtaining accurate K_{DP} estimates is challenging. Measurement error, phase folding, and scattering phase contributions introduce significant errors in K_{DP} estimation. K_{DP} is theoretically defined as the range derivative of the differential propagation phase (ϕ_{DP}) with $K_{DP} = \frac{1}{2}\frac{d\phi_{DP}}{dr}$, where r represents the distance from the radar. In practice, it is often estimated as the range derivative of the measured total differential phase $\widehat{\Phi}_{DP}$ ($\frac{d\widehat{\Phi}_{DP}}{dr}$) using least-square-fit (LSF) methods, which can introduce inaccuracies. However, $\widehat{\Phi}_{DP}$ contains not only ϕ_{DP}, but also measurement errors (ε) and the differential backscattering phase (δ). While ε can be mitigated through LSF and smoothing techniques, the presence of δ significantly affects $\widehat{\Phi}_{DP}$, leading to erroneous K_{DP} estimates. This issue is particularly pronounced in the case of hail and tornado debris, which exhibit non-Rayleigh scattering. Ignoring δ can result in unphysical K_{DP} values, such as unrealistically large or negative K_{DP}, leading to incorrect rainfall rate estimates (Giangrande and Ryzhkov 2008).

As detailed in Zhang (2016), the total differential phase from the phase of the co-polar cross-correlation function is expressed as $\Phi_{DP} = \phi_{DP} + \delta$, where ϕ_{DP} represents the differential

propagation phase and δ the differential backscattering phase. The measured total ϕ_{DP} ($\widehat{\phi}_{DP}$) includes measurement errors (ε), leading to $\widehat{\phi}_{DP} = \phi_{\mathrm{DP}} + \varepsilon = \phi_{\mathrm{DP}} + \delta + \varepsilon$ (Doviak and Zrnić 1993; Bringi and Chandrasekar 2001; Trömel et al. 2013; Kumjian 2013; Ralph-Hampton 2022). Falling hydrometeors typically align with their larger axis parallel to the ground, causing horizontally polarized waves to interact more with the hydrometeors than vertically polarized waves. This results in a larger propagation constant for horizontal polarization in rain, under the Rayleigh scattering approximation (Doviak and Zrnić 1993; Bringi and Chandrasekar 2001; Westbrook et al. 2010; Ralph-Hampton 2022). Consequently, intrinsic K_{DP} is expected to be positive, with ϕ_{DP} increasing monotonically along the radar beam in rain at S-band frequencies (Vivekanandan et al. 2001; Brandes et al. 2002). However, this behavior does not hold for other hydrometeors like hail, melting snow, and tornado debris, which scatter radar transmitted waves in non-Rayleigh scattering regime, causing errors in K_{DP} estimates.

Traditional methods to mitigate these errors have included iterative filtering (Hubbert and Bringi 1995), adaptive estimation techniques (Wang and Chandrasekar, 2009; 2010), and linear programming (LP) approaches that impose non-negativity constraints on K_{DP} (Giangrande et al., 2013). More recent hybrid LP approaches have incorporated self-consistency constraints at different radar bands, such as $K_{\mathrm{DP}}(Z_{\mathrm{H}}, Z_{\mathrm{DR}})$ at C-band (Huang et al. 2016; Aldana et al. 2024) and $\delta(Z_{\mathrm{DR}})$ at X-band (Otto and Russchenberg 2011; Schneebeli and Berne 2012; Geng and Liu 2023). Variational methods have also been explored to enhance K_{DP} estimation (Maesaka et al. 2012; Huang et al. 2021). While these methods have improved K_{DP} estimation, they often do not explicitly account for the differential backscattering phase (δ). For instance, Reimel and Kumjian (2021) focused on reducing measurement error (ε) by assuming Gaussian error distributions and idealized cases with no scattering phase contributions. However, in the presence of δ, ρ_{hv} decreases,

leading to larger fluctuations in $\widehat{\phi}_{DP}$, where the mean of these fluctuations with limited samples becomes non-zero. This inherent error persists regardless of the averaging or smoothing techniques applied, indicating that traditional methods may fall short in complex scattering environments.

The term 'KDP foot' has been used to describe areas within supercells showing enhanced K_{DP} (sometimes > 8° km^{-1}) in LSF-processed data from the WSR-88D network. This feature is often interpreted as an indicator of hail, particularly at its leading edge (Romine et al. 2008; Wilson 2019). However, the terminology and interpretation suggest a misunderstanding of K_{DP}'s nature. The 'KDP foot' is frequently misattributed to high liquid water content (Wilson and Van Den Broeke 2021), despite the likelihood that significant δ contributions from hail are the primary cause. Therefore, referring to this feature as a 'KDP foot' is misleading, as it conflates true K_{DP} with artifacts from δ, especially in melting hail scenarios. As shown in Figure 1, the idea that abnormally large K_{DP} values can be attributed to the physical properties of hail has been incorporated into the National Oceanic and Atmospheric Administration's Warning Decision Training Division's Radar Application Course on Dual-Pol Hail Analysis (WDTD 2025). While the operational calculation of K_{DP} does indeed produce values exceeding 10° km^{-1}, there is no mention of the potential influence of δ on these elevated values. As a result, this reinforces the incorrect notion that such high values are solely due to differential propagation phase rather than an artifact introduced by differential backscattering. The erroneous K_{DP} yields unrealistic large (~300 mm/hr) or negative values for rain rate estimation, which is not reasonable.

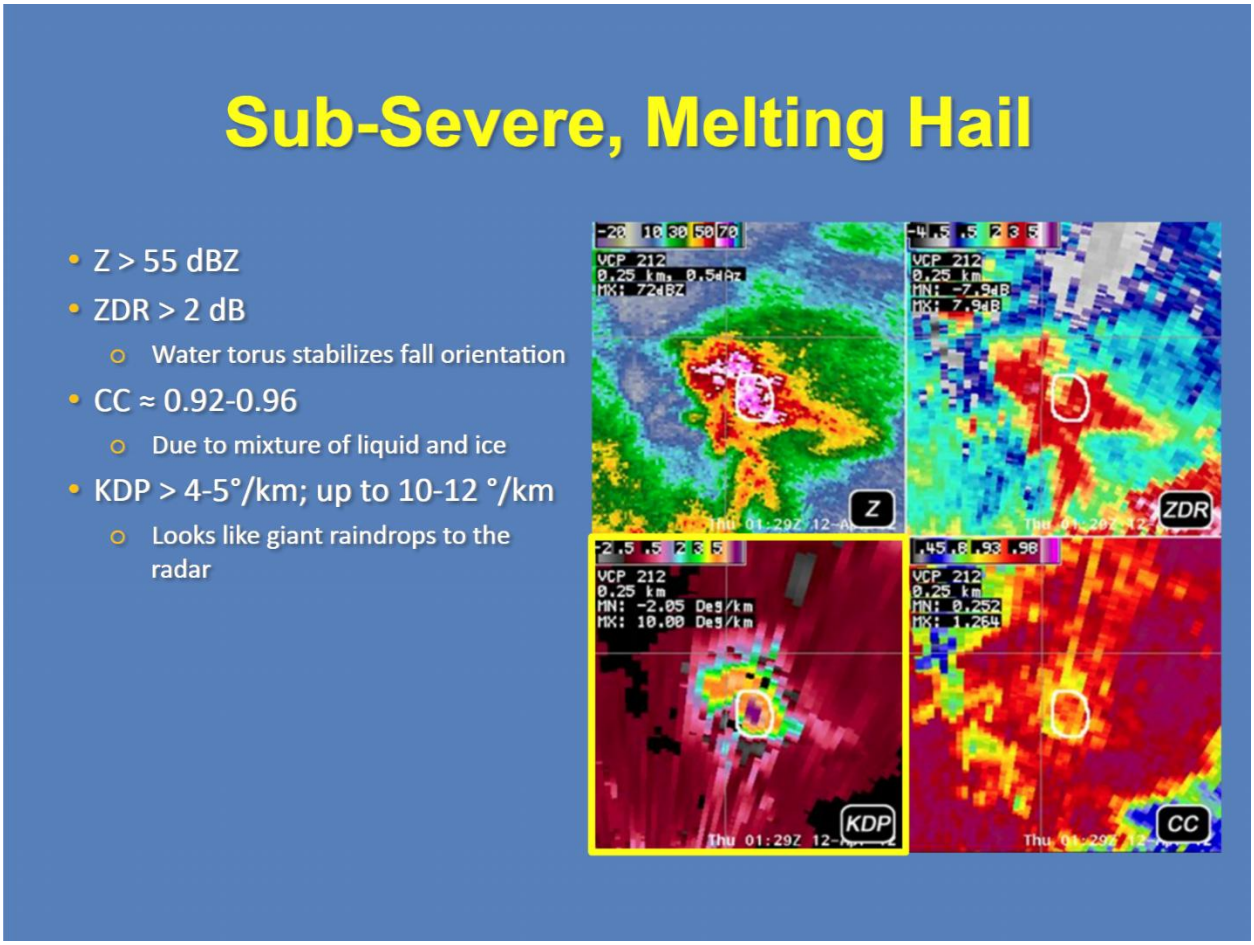


Figure 1: Slide from WDTD radar application course on hail detection (WDTD 2025).

Various methods have been proposed to tackle these challenges (Ryzhkov et al. 2005a; Wang and Chandrasekar 2009; Otto and Russchenberg 2011). Linear programming (LP) has proven effective in minimizing δ's influence, maintaining a monotonic ϕ_{DP} increase and producing non-negative, unbiased K_{DP} profiles in rain regimes (Giangrande et al. 2013; Huang et al. 2016). Although computationally intensive, advancements in computing power have made LP a viable option. Using $\widehat{\Phi}_{DP}$ and linear constraints, LP derives an optimized ϕ_{DP} profile closely matching $\widehat{\Phi}_{DP}$. Giangrande et al. (2013) found that LP estimation of K_{DP} has a mean bias error of 0.1° km^{-1}, compared to 0.18° km^{-1} for LSF estimation. Given LP's success in rain regimes, it is reasonable to apply it to Rayleigh scattering regimes for realistic radial profiles of ϕ_{DP} and K_{DP}. Additionally,

applying LP to Rayleigh scattering along a radial profile enables δ estimation in non-Rayleigh regimes. Truly addressing these challenges requires processing techniques that separate δ from ϕ_{DP}, enabling more accurate K_{DP} estimation and better precipitation microphysics characterization. Improved K_{DP} estimates will enhance precipitation measurements and provide valuable insights into hydrometeor properties. In this study, we introduce a novel methodology that employs classification-based linear optimization to estimate both ϕ_{DP} and δ, within regions of Rayleigh and non-Rayleigh scattering. By focusing on Rayleigh scattering regimes, where particles are small relative to the radar wavelength, we aim to reduce the influence of complex scattering effects and improve the accuracy of our estimates. This approach leverages the physical characteristics of Rayleigh scatterers to enhance the reliability of polarimetric radar measurements.

Previous studies have explored the relationship between scattering phase signatures and non-Rayleigh scatterers (Balakrishnan and Zrnic 1990, Melnikov et al. 2015, Tremol et al. 2014), while others have suggested that these signatures may be artifacts of non-uniform beam filling (Ryzhkov et al. 2005a). We propose that in scenarios where a radar beam samples pure Rayleigh regime scatterers, there should be no expected difference in the phase contributions between the horizontally and vertically polarized waves beyond the propagation effects, meaning δ should be negligible. Consequently, any significant deviations in the measured differential phase ($\widehat{\Phi}_{\mathrm{DP}}$) can be attributed primarily to measurement errors (ε) rather than backscattering effects. This understanding allows us to refine our linear optimization techniques to isolate δ in non-Rayleigh scattering environments by establishing a robust baseline in Rayleigh regimes. By accurately distinguishing between ϕ_{DP} and δ, this methodology promises to enhance the reliability of polarimetric radar data, ultimately improving precipitation estimation, hydrometeor classification, and severe weather detection.

2. Background

A radar system operates by transmitting an electromagnetic wave of known frequency, duration, polarization, and power, directing the signal in a specific direction using an antenna. The system then measures the amplitudes and phases of the returning signals, which results from backscattering off atmospheric targets. Radar technology saw significant advancements during the Second World War, driven by the military's need to detect enemy aircraft and submarines. Meteorologists, who played a crucial role in military operations due to the strategic importance of weather forecasting, quickly recognized radar’s potential for meteorological applications. This realization marked the beginning of weather radar technology.

Electromagnetic waves are characterized by four fundamental properties: wavelength/frequency, amplitude, phase, and polarization. Wavelength, the distance between successive wave peaks, is approximately 10 cm for NEXRAD systems. Frequency, the number of oscillations per second, is inversely proportional to wavelength, while amplitude, the maximum displacement of the wave, is related to the energy it carries. Phase describes the position of the wave within its oscillation cycle and plays a critical role in radar measurements. Polarization is the direction of wave vibration (field).

When electromagnetic waves encounter atmospheric particles, a portion of the energy is scattered in different directions. Some of this energy is backscattered toward the radar, where it is measured. The strength of the returned signal depends on the size, shape, and composition of the scatterer. This interaction is commonly described using the radar cross-section (RCS), which quantifies how effectively a target scatters energy back to the radar. For dielectric spheres, the RCS follows Mie theory (Mie 1908), which explains how the relationship between radar waves and spherical particles varies with particle size. When the scatterer’s diameter is much smaller

than the radar wavelength—less than approximately $\frac{\lambda}{16}$ (6.25 mm for NEXRAD systems)—the backscattered power is proportional to the sixth power of the particle diameter. This relationship enables the definition of the reflectivity factor (also called as radar reflectivity) as the 6^{th} moment of raindrop size distribution, and hence its relation to precipitation intensity. However, as the particle size approaches the radar wavelength, complex interactions arise due to constructive and destructive interference, leading to oscillations in the returned signal strength such that this simple definition/relationship of radar reflectivity is no longer valid.

As the transmitted wave propagates through the atmosphere, it undergoes attenuation, a systematic reduction in signal strength due to scattering and absorption. Attenuation is particularly significant in regions of heavy precipitation, which weaken the transmitted wave before it returns to the radar (Doviak and Zrnić 1993). The presence of hydrometeors also causes additional phase shift for wave propagation in the atmosphere.

Understanding these fundamental wave interactions is essential for interpreting radar measurements. Before examining the additional insights provided by dual-polarization radar, we must first establish a foundation in the traditional Doppler radar variables: reflectivity, radial velocity, and spectrum width. The following sections will explore each of these variables in depth, highlighting their role in detecting and analyzing atmospheric phenomena.

2.1 Single polarization radar variables

2.1.1. Reflectivity

Reflectivity is a fundamental measurement in weather radar, representing the power of the returned radar signal and providing insight into precipitation intensity. Specifically, reflectivity in a given polarization is proportional to the received power in that polarization divided by the

transmitted power, yielding values in linear units of $mm^6\ m^{-3}$ (Fabry 2015). Since this scale covers a wide range—from 0.01 $mm^6\ m^{-3}$ in liquid clouds to over 10^6 $mm^6\ m^{-3}$ in hail—the reflectivity factor is commonly expressed in logarithmic units (decibels), defined as

$$Z_{\mathrm{H,V}} = 10log_{10}\left(Z_{\mathrm{h,v}}\right), \tag{2.01}$$

where liquid clouds exhibit around -20 dBZ and hail can reach 60 dBZ (Fabry 2015). In Rayleigh scattering, the reflectivity factor is closely tied to the drop size distribution (DSD) of hydrometeors and is mathematically represented as:

$$Z = \int D^6 N(D) dD, \tag{2.02}$$

where N(D) is the number of droplets with diameter D within a unit volume per unit diameter (Kessler 1969). However, this is specifically valid for a drop size distribution (DSD) of rain as (2.02) is normalized to the dielectric constant of water as well as the radar wavelength. Due to the D^6 dependence, larger droplets disproportionately influence reflectivity, which is why a single 2 mm droplet has a similar reflectivity factor to 64 droplets of 1 mm diameter (Fabry 2015). This introduces challenges when estimating rainfall rates, as larger drops contribute more to reflectivity but not necessarily to total rainfall. Marshall and Palmer (1948) first demonstrated that rainfall rate is influenced by the DSD, leading to empirical relationships of the form $Z=aR^b$, where R is the rain rate. These relationships vary regionally due to differing microphysical and dynamical processes (Stout & Mueller 1968; Smith & Krajewski 1993; Amitai 2000; Kim et al. 2021). Reflectivity is also sensitive to factors such as radar calibration, radome moisture (Schneebeli et al. 2012; Mancini et al. 2018), beam blockage from terrain or buildings, and signal attenuation. For spherical rain particles, the radar reflectivity factor has been further expanded to account for polarization effects, varying particle shapes and orientations, and variability in DSD (Danielsen et

al. 1972; Smith et al. 1975; Doviak & Zrnić 1993; Zhang 2016). When Rayleigh scattering conditions are not met, the reflectivity factor is expressed as:

$$Z_{h,v} = \frac{4\lambda^4}{\pi^4 |K_{\mathrm{w}}|^2} \int_0^\infty \left| s_{\mathrm{hh,vv}}(\pi, D) \right|^2 N(D) dD \tag{2.03}$$

where K_w is the dielectric constant factor of water and s_{hh} and s_{vv} are the backscattering amplitudes for horizontal and vertical polarizations, respectively (Doviak & Zrnić 1993, Zhang 2016).

2.1.2. Radial Velocity

Radial velocity, or Doppler velocity, leverages the Doppler shift principle to quantify the motion of targets either toward or away from the radar. As targets move within the radar's sampling volume, the phase of the returned electromagnetic wave shifts slightly between successive measurements of the same location. This phase shift corresponds to the mean movement of the targets within that volume. By precisely measuring these incremental phase changes between consecutive pulses, the Doppler velocity is determined from the phase of the auto-correlation function of radar signals (Doviak & Zrnić 1993). Doppler velocity is defined conventionally with positive values representing motion away from the radar and negative values indicating motion toward it. This measurement depicts the mean radial velocity of scatterers within the radar's resolution volume, providing critical insight into atmospheric motion. However, it only captures one component of the three-dimensional wind field—specifically, the component along the radar beam's axis. To reconstruct the complete wind field, additional data from different viewing angles are required. One common approach involves utilizing a second Doppler radar positioned at a different location to obtain overlapping measurements, allowing for a comprehensive depiction of the wind field structure (Trapp et al. 2020). This method of dual-Doppler analysis has proven invaluable in meteorological studies, offering detailed insights into

complex phenomena such as tornadoes, mesoscale convective systems, and other severe weather events. By integrating multiple perspectives, researchers can derive horizontal and vertical wind components, facilitating a more complete understanding of atmospheric dynamics (Bluestein & Wakimoto 2003; Gao et al. 2013).

2.1.3. Spectrum Width

Spectrum width represents the variability in the radial velocities of scatterers within a radar resolution volume. Unlike Doppler velocity, which provides the mean radial velocity of the targets, spectrum width quantifies the spread of these velocities, reflecting the degree of motion diversity among the scatterers. The principle behind spectrum width is rooted in the fact that not all targets within a sampled volume move at the same speed. These variations in velocity cause fluctuations in the Doppler velocity measurements over successive radar pulses, as the phase interference patterns shift slightly between returns. The rate of these fluctuations is defined as the spectrum width, providing insight into the range of velocities present within the volume. Turbulence is generally considered the primary contributor to spectrum width, as it induces random, chaotic motions among particles within the radar's sampling volume (Istok & Doviak 1986). However, several other factors can also influence spectrum width, including:

- Wind shear: Variations in wind speed and direction across the resolution volume can increase the spread of velocities.
- Differences in hydrometeor fall speeds: Hydrometeors of varying sizes and densities fall at different rates, contributing to velocity dispersion.

- Changes in hydrometeor orientation: While this is a minor and indirect effect, fluctuations in the orientation of non-spherical hydrometeors can affect the phase characteristics of the returned signal, indirectly impacting spectrum width (Li & Zhang 2022).

- Clutter contamination: Spectrum width can serve as a useful indicator for identifying ground clutter in radar data. Since many ground clutter targets—such as buildings and terrain—are stationary, they exhibit near-zero radial velocity and near-zero spectral broadening. As a result, both the Doppler velocity and spectrum width are typically very low for these fixed targets. For example, a radar return from a building would generally appear as a zero-velocity, zero-spectrum-width signal. However, not all ground clutter behaves in a completely static manner. Clutter sources like trees or other vegetation can sway in response to ambient wind, introducing some degree of motion and resulting in a small, but non-zero, spectrum width. Still, this type of clutter typically exhibits spectrum width signatures that are distinguishable from those of true meteorological targets.

Understanding spectrum width is crucial in diagnosing atmospheric turbulence and wind shear, particularly within convective systems. Enhanced spectrum width values can indicate turbulent zones, aiding in the detection of hazardous weather phenomena like microbursts or tornadoes. Moreover, when combined with Doppler velocity data, spectrum width provides a more comprehensive view of the atmospheric dynamics within a given radar volume.

2.2. Dual-polarization variables

Doppler variables form the foundation of radar meteorology, providing crucial information about storm intensity, wind, wind shear, and turbulence. However, they offer limited insight into the microphysical properties of precipitation. A major advancement in radar technology—dual-polarization radar—has significantly enhanced our ability to analyze precipitation by transmitting

and receiving electromagnetic waves in both horizontal and vertical polarizations (Kennaugh 1952; Huynen 1970; McCormic and Henrdy 1975; Seliga and Bringi 1976; Boerner et al. 1981). Traditional single-polarization radars could only measure the power and phase of returned signals in a single orientation, whereas dual-polarization systems compare signals from both polarizations. This additional dimension of information improves the identification of hydrometeor types, distinguishing rain, hail, snow, and melting precipitation with far greater accuracy.

For ground-based remote sensing, radar polarimetry is both cost-effective and efficient in retrieving detailed microphysical information about precipitation (Seliga and Bringi 1976; Seliga et al. 1979; Zrnić and Aydin 1992; Zhang 2019). Recognizing these benefits, the National Weather Service completed a major upgrade to the NEXRAD radar network in the summer of 2013, incorporating dual-polarization capabilities to improve meteorological observations (Doviak et al. 2000). These enhancements enable better delineation of precipitation types (e.g., rain, snow, and hail), improve the accuracy of quantitative precipitation estimation, and facilitate the detection of tornado debris signatures—critical for severe weather analysis and warnings (Ryzhkov et al. 2005; Kumjian 2013b; Stepanian 2016).

To understand the fundamentals of dual-polarization, consider an electromagnetic pulse propagating from the radar toward a collection of scatterers. The pulse consists of two orthogonal wave components—one oscillating in the horizontal plane and the other in the vertical plane. When multiple waves of the same polarization interact within a given space, they sum coherently, meaning both their amplitude and phase contribute to a resultant wave. It is the resultant wave that the radar interprets returning signals, providing valuable insights into the size, shape, and orientation of atmospheric scatterers.

Furthermore, the way electromagnetic waves propagate through precipitation depends on polarization. In a uniform cloud of spherical droplets, both horizontal and vertical waves experience equal attenuation. However, in a field of oblate raindrops, horizontal polarization undergoes greater interaction and attenuation than vertical polarization due to the larger effective cross-section. We illustrate this concept in Figure 2.

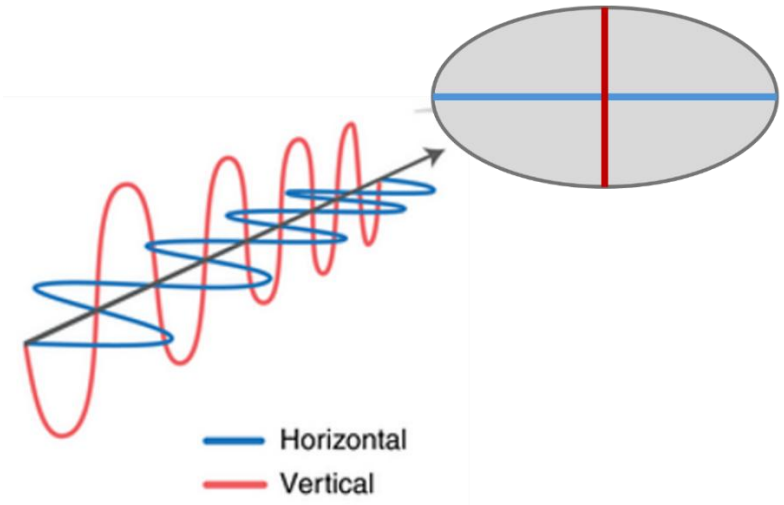


Figure 2: Polarized wave with traces of the horizontal polarization (blue) and vertical polarization (red) propagating toward an oblate sphere representing a droplet with the projection of the two polarization onto their respective cross-sections on the drop.

Along with differential attenuation, this introduces phase shifts between the two polarizations—one of the key principles leveraged in dual-polarization radar to infer microphysical properties of precipitation. Accounting for the effects of propagation and scattering alters how we express polarimetric radar variables. For instance, with the effects included, we can express radar reflectivity factor per of Zhang (2016):

$$Z'_{\mathrm{H}} = Z_{\mathrm{H}} - 2\int_0^r A_{\mathrm{H}}(l)dl \equiv Z_{\mathrm{H}} - PIA_{\mathrm{H}} \tag{2.04}$$

where $PIA_{\mathrm{H}} \equiv 2\int_0^r A(l)dl$ stands for the two-way path-integrated attenuation. The negative sign out front of PIA_{H} the energy loss between the radar location and target for the propagating wave.

With this foundation in place, we now turn to the suite of additional radar products enabled by dual-polarization technology, which extend beyond the capabilities of traditional Doppler variables.

2.2.1. Differential Reflectivity

Prior to the NEXRAD upgrade to dual polarization, radar reflectivity factor (Z_H) was measured only at horizontal polarization, providing information on the aerial density and size of scatterers in the horizontal dimension. With dual polarization, reflectivity can be measured for both horizontal (Z_H) and vertical (Z_V) polarizations, allowing for the calculation of differential reflectivity (Z_{DR}). Differential reflectivity is defined as the logarithm of the ratio of reflectivity factors in the horizontal and vertical polarizations:

$$Z_{\mathrm{DR}} = 10 \log_{10} \left(\frac{Z_{\mathrm{h}}}{Z_{\mathrm{v}}} \right). \tag{2.05}$$

Expressed in decibels (dB), Z_{DR} provides insight into the shape and orientation of hydrometeors. For Rayleigh scatterers, Z_{DR} is related to the axis ratio of particles, with large positive values indicating oblate (horizontally oriented) scatterers, large negative values indicating prolate (vertically oriented) scatterers, and near-zero values indicating spherical or randomly oriented scatterers (Rinehart, 2010). With the effects of propagation and scattering included, we can express Z_{DR} per equation (4.140) of Zhang 2016:

$$Z'_{\mathrm{DR}} = Z_{\mathrm{DR}} - 2 \int_0^r A_{\mathrm{DP}}(l) dl \equiv Z_{\mathrm{DR}} - PIA_{\mathrm{H}} \tag{2.06}$$

where $PIA_{\mathrm{DP}} \equiv 2 \int_0^r A(l) dl$ stands for the two-way path-integrated differential attenuation. As previously mentioned, the horizontal polarization typically experiences greater interaction with the scatterer than the vertical polarization. This results in a positive PIA_{DP}, leading to a negative bias

in differential reflectivity. This effect is particularly important to account for at shorter wavelengths, such as C-band and X-band.

In rain, Z_{DR} typically increases with increasing raindrop size since larger drops tend to be more oblate due to aerodynamic forces (Seliga & Bringi 1976). The use of Z_{DR} for quantitative precipitation estimation (QPE) and drop size distribution (DSD) retrievals has been well documented (Seliga et al. 1979; Ulbrich & Atlas 1984; Zhang et al. 2001; Cao et al. 2008). Z_{DR} also provides insight into precipitation regimes. Continental rain, which tends to have larger raindrops, often exhibits higher Z_{DR} compared to tropical rain, which generally has smaller drops (Ryzhkov et al. 2005b; Tokay et al. 2008; Ryzhkov et al. 2011). In convective storms, size sorting can lead to high Z_{DR} with relatively moderate Z_H in leading convective regions (Kumjian et al. 2013). In frozen hydrometeors, Z_{DR} behavior varies. Hail often exhibits low Z_{DR} due to its tumbling motion, which randomizes its orientation (Aydin & Zhao 1990; Picca & Ryzhkov 2012). In contrast, vertically aligned ice crystals, sometimes found in strong electric fields, can produce negative Z_{DR} (Willmarth et al. 1964; Westbrook et al. 2010). Unlike reflectivity, Z_{DR} is less affected by absolute miscalibration of the radar system, as calibration errors tend to affect both polarizations equally (Kumjian, 2013).

2.2.2. Co-Polar Correlation Coefficient

The co-polar correlation coefficient (ρ_{hv}) quantifies the similarity between the horizontally and vertically polarized backscattered signals within a given radar sampling volume. ρ_{hv} represents the degree of similarity in phase and amplitude fluctuations of the two polarized backscatter signals over multiple radar pulses. Mathematically, the intrinsic value is defined as:

$$\rho_{hv} = \frac{\left| \int s_{hh}^{*}(\pi, D) s_{vv}(\pi, D) N(D) dD \right|}{\left[\int |s_{hh}(\pi, D)|^2 N(D) dD \int |s_{vv}(\pi, D)|^2 N(D) dD \right]^{\frac{1}{2}}} \tag{2.07}$$

where s_{hh} and s_{vv} are the complex scattering amplitudes at horizontal and vertical polarizations, respectively, and N(D) is the drop size distribution (Doviak et al. 2000). However, (2.07) provides the intrinsic value of ρ_{hv}. When taking account the propagation effects, we can express ρ_{hv} as follows from Zhang (2016):

$$\tilde{\rho}'_{hv} = \frac{\langle n s'^{*}_{hh} s'_{vv} \rangle}{\sqrt{\langle n|s'_{hh}|^2 \rangle \langle n|s'_{vv}|^2 \rangle}} = \frac{\langle n s^{*}_{hh} s_{vv} \rangle}{\sqrt{\langle n|s_{hh}|^2 \rangle \langle n|s_{vv}|^2 \rangle}} e^{-2\int_0^r \mathrm{Re}(K_h - K_v) dl}$$

$$= \tilde{\rho}_{hv} e^{-2\int_0^r \mathrm{Re}(K_h - K_v) dl} = \rho_{hv} e^{-j\delta_{hv}} e^{-j\phi_{dp}} \quad (2.08)$$

where $\delta_{hv} = \bar{\delta}_h - \bar{\delta}_v$ is the difference between the mean backscattering phase of the horizontal and vertical polarizations. Thus, (2.08) shows that the measured co-polar correlation coefficient is dependent on the forward scattering properties of hydrometeors along the path to and from the radar resolution volume as well as within the volume itself. Furthermore, (2.08) shows us that while the magnitude of the correlation coefficient with propagation effects (ρ'_{hv}) is equal to that without propagation effects (ρ_{hv}), the correlation phases are related by the following:

$$\phi_{DP} = \delta + \phi_{DP}(r) = \frac{180}{\pi}\left(\delta_{hv} + \phi_{dp}\right) \quad (2.09)$$

Equation (2.09) expresses the total differential phase which will be discussed in the following section.

In a homogenous sampling volume with identical scatterers, $\rho_{hv} = 1$, indicating perfect correlation between the two polarizations. However, when the scatterers exhibit variability in size, shape, orientation, or phase, ρ_{hv} decreases (Sachidananda & Zrnić 1989). This reduction can occur due to:

- Random non-Rayleigh scattering: Wave scattering in non-Rayleigh regime by hail, melting snow and biological scatterers yields scattering phase which is random and different for different polarizations, cause reduced ρ_{hv} (Zhang 2016).
- Hydrometeor Diversity: Variability in the types, sizes, or orientations of scatterers lowers ρ_{hv} (Kumjian 2013).
- Turbulence & Advection: Motion of scatterers through the volume, particularly in strong wind shear or convective updrafts, disrupts polarization consistency, reducing ρ_{hv} (Ryzhkov & Zrnić 2019).
- Non-Uniform Beam Filling (NBF): Consider a resolution volume where scatterers are significantly more concentrated in one section than in another. As the radar beam propagates through this volume, one portion of the beam undergoes greater phase reduction than the other. As shown in Eq. (2.08), this differential propagation phase leads to a decrease in the measured ρ_{hv}, a phenomenon known as non-uniform beam filling. Similarly, the presence of differential backscattering phase can produce a comparable effect. Thus, if the radar beam contains a mixture of scatterer types across the sampling volume, the measured ρ_{hv} decreases due to the spatial inhomogeneity in scattering properties (Ryzhkov 2007), however this is not the case if all scatterers are in the Rayleigh scattering regime in which there is no differential scattering phase.

ρ_{hv} serves as a fundamental metric for hydrometeor classification. High values ($\rho_{\mathrm{hv}} > 0.98$) are characteristic of rain at S-band frequencies due to the consistent shape and orientation of raindrops (Kumjian 2013; Ryzhkov & Zrnić 2019). Lower values (~0.85–0.95) result from irregularly shaped, tumbling hailstones, which cause depolarization (Aydin & Zhao 1990).

Biological scatterers (insects or birds) can cause $\rho_{\mathrm{hv}} \sim 0.6$ or even lower. Lofted debris produces extremely low values ($\rho_{\mathrm{hv}} < 0.4$), distinguishing it from meteorological scatterers. The U.S. National Weather Service uses this signature to confirm tornadic activity (Ryzhkov et al. 2005c; Houser et al. 2016).

2.2.3. Differential Phase

The differential phase (ϕ_{DP}) is one of the fundamental polarimetric radar variables, providing key insights into the microphysical properties of clouds and precipitation and the propagation effects experienced by radar waves. Unlike reflectivity-based parameters, which describe the intensity of scattered power, ϕ_{DP} directly relates to the phase difference accumulated between horizontally and vertically polarized waves as they traverse a medium. This accumulation occurs because oblate raindrops, typically oriented with their larger axis parallel to the ground, cause the horizontal wave to have greater interaction with the hydrometeor than a vertically polarized wave, yielding a larger propagation constant (or wave number) for horizontal polarization in rain when the Rayleigh scattering approximation is valid, such that the horizontal wave travels more slowly and leading to a net increase along the beam path (Doviak and Zrnić 1993, Bringi and Chandrasekar 2001; Westbrook et al. 2010; Ralph-Hampton 2022). This measured value is typically reported as an angle between 0° and 360° (Melnikov et al. 2015). However, the total phase difference measured by radar ($\widehat{\phi}_{DP}$) includes not only propagation effects but also contributions from radar hardware and scattering interactions. As shown in Eq. (4.144) of Zhang (2016), the total differential phase from the phase of the co-polar cross correlation function is given by Eq. (2.09) and thus, the total measured differential phase ($\widehat{\phi}_{\mathrm{DP}}$) includes the addition of measurement error yielding

$$\widehat{\Phi}_{\mathrm{DP}} = \Phi_{\mathrm{DP}} + \varepsilon = \phi_{DP} + \delta + \varepsilon \quad (2.10)$$

(Doviak and Zrnić 1993, Bringi and Chandrasekar 2001; Trömel et al. 2013; Kumjian 2013; Ralph-Hampton 2022). The first term on the right-hand side of the equation (ϕ_{DP}) is the differential propagation phase, accumulated as the radar beam moves toward and returns from a scatterer and resulting from differences in the forward propagation of horizontally and vertically polarized waves. The second term (δ) is the differential backscattering phase, caused by asymmetric scattering from targets and introduced when the beam interacts with non-Rayleigh scatterers, such as hail, tornado debris, biological scatterers, or melting hydrometeors. Finally, ε represents measurement error, error from hardware, sampling, and other uncertainties. We illustrate these components in Figure 3 where $\widehat{\Phi}_{\mathrm{DP}}$ is shown by the blue line, and an estimated ϕ_{DP} is shown by the red line. From approximately 36-55 km we see an easily identifiable Rayleigh scattering regime where the mean $\widehat{\Phi}_{\mathrm{DP}}$ is mainly monotonically increasing and we see fluctuations around the mean from the presence of ε. Farther down radial, from approximately 55-65 km, we see a well-defined 'bump' in the $\widehat{\Phi}_{\mathrm{DP}}$. Though there still exist small oscillations in the measurements from gate to gate, the uniformity of this structure suggests the contribution of δ found in non-Rayleigh scattering regimes. We will more comprehensively analyze this radial in the context of its environment in the Results section.

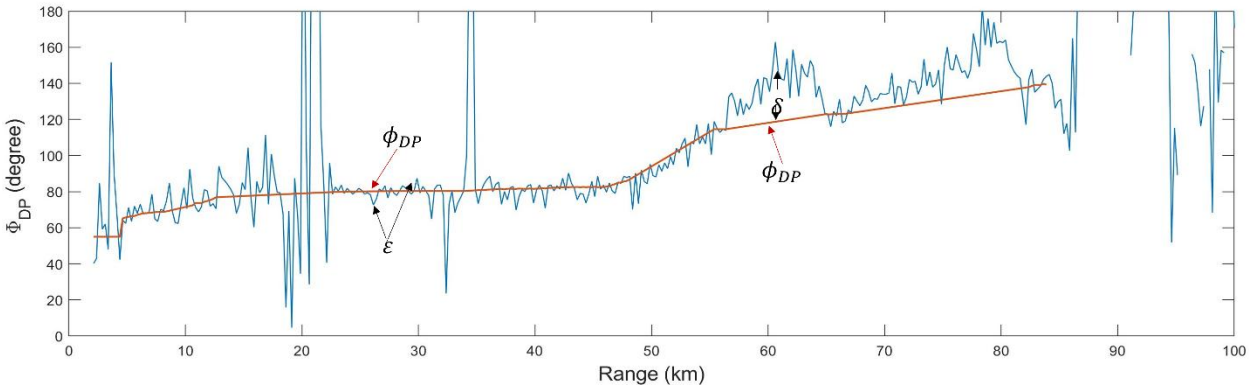


Figure 3: Measured radial profile of differential phase (blue) with estimation of ϕ_{DP} (red) and illustrations of δ and ε contained in the measurement.

2.2.4. Specific Differential Phase

Propagation effects in a medium can be described using an effective complex wave number (K) or an effective refractive index (m), given by (Zhang 2016):

$$m = \sqrt{\varepsilon_e} \tag{2.11}$$

$$K = km \tag{2.12}$$

where ε_e represents the effective dielectric constant of the medium, and k is the idealized wave number in free space for a given wavelength. The presence of particles in the medium increases the wave number and decreases the wavelength, thereby slowing wave propagation. This leads to a phase shift in the propagating wave, which is characterized by the specific phase—the rate of phase change per unit distance.

When a polarized wave propagates through a medium containing nonspherical particles, the wave fields in the horizontal and vertical polarizations experience different propagation constants (K_h and K_v). Since most atmospheric particles tend to align with their major axes parallel to the ground, the horizontal polarization interacts more strongly with the scatterers than the vertical polarization. As a result, the difference between the effective propagation constants

(K_h - K_v) is typically positive, especially in pure rain regimes. The specific differential phase (K_{DP}) is defined as (Zhang 2016):

$$K_{DP} = \frac{180}{\pi}\mathrm{Re}[K_h - K_v] \approx \frac{180\lambda}{\pi}\int \mathrm{Re}[s_a(0,D) - s_b(0,D)]N(D)dD\frac{1}{2}\left(1 + e^{-2\sigma_\vartheta^2}\right)e^{-2\sigma_\varphi^2} \quad (2.13)$$

where $\mathrm{Re}[K_h - K_v]$ represents the real part of the differential propagation constants, with units of degrees per kilometer.

As a radar beam propagates through a medium, the phase of each polarization changes due to variations in the propagation environment. The two-way accumulated differential phase due to forward propagation, denoted as $\phi_{DP} = 2\int_0^r K_{DP}(r')dr'$, increases with the range (r). Since it is often more useful to assess how this phase difference changes at a specific location along the radar beam's path, specific differential phase is related to the range derivative of ϕ_{DP} by:

$$K_{DP} = \frac{1}{2}\frac{d\phi_{DP}}{dr} \quad (2.14)$$

K_{DP} represents the difference in phase change rates between horizontally and vertically polarized waves as they traverse clouds and precipitation (Attisani et al. 1974; Chu 1974; McCormic and Hendry 1975; Oguchi 1977; Seliga and Bringi 1978). Because K_{DP} arises from differential forward propagation, it provides valuable microphysical information about cloud/precipitation particles. It is particularly beneficial for quantitative precipitation estimation (QPE) due to its close to linear relation with rain rate and its independence from absolute power measurements. Unlike reflectivity (Z_H) and differential reflectivity (Z_{DR}), K_{DP} is a phase-based measurement, making it immune to radar miscalibration, attenuation, and partial beam blockage (Seliga and Bringi 1978; Kumjian 2013). Consequently, numerous studies have explored its use in rainfall estimation, both independently and in combination with Z_H and Z_{DR} (Aydin et al. 1995; Zrnić and Ryzhkov 1996; Matrosov et al. 2006).

2.2.5. Overview of Polarimetric Radar Variables

To help readers unfamiliar with polarimetric radar, the table below summarizes each of the key polarimetric variables used in this study. It outlines what each variable measures, its practical advantages and limitations, and where it's most useful in hydrometeor identification.

Table 1: Radar Variable Quick Reference Table for Non-Specialists

Variable	**What It Measures**	**Advantages**	**Limitations**	**Most Useful For**
$\mathbf{Z_H}$ (Reflectivity)	Returned power from horizontally polarized wave	Good for estimating rainfall rate and identifying intense storms	Doesn't distinguish shape/hydrometeor type	Storm Intensity
$\mathbf{Z_{DR}}$ (Differential Reflectivity)	Difference in return power between H and V polarizations	Helps distinguish shape and orientation of hydrometeors	Sensitive to mis-calibration and differential attenuation	Hydrometeor type/drop size
$\boldsymbol{\rho_{hv}}$ (Correlation Coefficient)	Correlation between H and V polarized signals	Helps determine uniformity of scatterers	Small dynamic range, difficult to use quantitatively	Data quality control, clutter and debris detection, hydrometeor classification
$\mathbf{\Phi_{DP}}$ (Differential Phase)	Phase shift difference between H and V polarized waves	Immune to calibration bias, works well in heavy rain	Path-integrated quality, can be difficult to interpret	Rainfall accumulation estimation, attenuation correction
$\mathbf{K_{DP}}$ (Specific Differential Phase)	The change rate of differential propagation phase	Close to a linear relation with rainrate, good for estimating rainfall in heavy precipitation	Difficult to estimate accurately in the presence of non-Rayleigh scatterers (e.g., melting snow, hail, tornado debris…)	Quantitative Precipitation Estimation (QPE), microphysics retrieval

2.2 Simulation of Scattering Properties

To gain a deeper understanding of the estimation and application of K_{DP} and δ, it is essential to examine both parameters within a theoretical framework. The plots in Figure 4 and Figure 5 were generated using the T-matrix method (Waterman 1965; Vivekanandan et al. 1991) to illustrate the backscattering magnitude, backscattering phase, and the real part of the forward scattering amplitude. These results are presented for both major and minor axis polarizations and correspond to hailstones at various stages of melting, expressed as a percentage of melting, plotted as a function of the equivolume diameter. In this study, hailstones were modeled as oblate spheroids with an axis ratio of 0.7. Their dielectric constants were computed using both the Maxwell-Garnett (M-G) mixing formula and the Polder-van Santen (P-S) mixing formula to account for variations in the composition of melting hailstones.

Hydrometeors, with the exception of rain, often exist as mixtures of two or more materials. Melting hailstones, for instance, consist of both ice and water. In a two-material system, one can conceptualize the scenario where a number of small spheres of one material are embedded within a background medium of the other. Each of these materials possesses a unique dielectric constant, which quantifies the material's ability to polarize in response to an applied electric field (Zhang 2016). When subjected to an electric field, the positive and negative charges in a material shift slightly, creating tiny dipoles—a process known as polarization. A material's dielectric constant reflects the extent to which it slows and weakens the electric field relative to a vacuum.

To estimate the effective dielectric constant (ε_e) of a two-component mixture, the Maxwell-Garnett (M-G) mixing formula provides an analytical expression, as given in Zhang (2016):

$$\varepsilon_e = \frac{1 + 2fy}{1 - fy}\varepsilon_1 \tag{2.15}$$

with

$$y = \frac{\varepsilon_2 - \varepsilon_1}{\varepsilon_2 + 2\varepsilon_1} \tag{2.16}$$

In this formulation, *f* represents the fractional volume of the inclusions (embedded material) within the background medium, while ε_1 and ε_2 correspond to the dielectric constants of the background and inclusion materials, respectively. The resulting ε_e is thus a weighted combination of the background and inclusions, where an increase in *f* enhances the influence of the inclusions on ε_e. However, the M-G formula is only valid when $fy \ll 1$, as it is derived under the assumption that the embedded spheres contribute less to ε_e than the background medium. Therefore, selecting the appropriate background and inclusion material is crucial, taking into account their respective contributions with combined effects of fractional volumes and dielectric properties.

In some cases, neither material necessarily dominates the effective dielectric properties. Instead, it may be more appropriate to treat both materials as inclusions embedded within an effective medium, where the polarizabilities of both components contribute to the overall response with respect to the effective medium. This approach is described by the Polder-van Santen (P-S) mixing formula, given in Zhang (2016) as:

$$f_1 \frac{\varepsilon_1 - \varepsilon_e}{\varepsilon_1 + 2\varepsilon_e} + f_2 \frac{\varepsilon_2 - \varepsilon_e}{\varepsilon_2 + 2\varepsilon_e} = 0 \tag{2.17}$$

Here, f_1 and f_2 denote the fractional volumes of the two constituent materials, which together must sum to unity. Since the P-S formula allows for a higher fraction of inclusions, it is often preferred when modeling densely packed hydrometeors, where interactions between inclusions significantly influence the effective dielectric constant.

Given that hail is commonly found in a partially melted state, our simulations explored a range of possible ε_e values corresponding to different degrees of melting. Specifically, we

examined cases with 20% (Figure 4) and 40% (Figure 5) melting. For each scenario, we considered both ice and water as the background medium, treating the other component as the inclusion per the M-G formula. These results were then compared to the P-S mixing formula and the case of completely dry hail to assess the differences in scattering properties under varying dielectric assumptions.

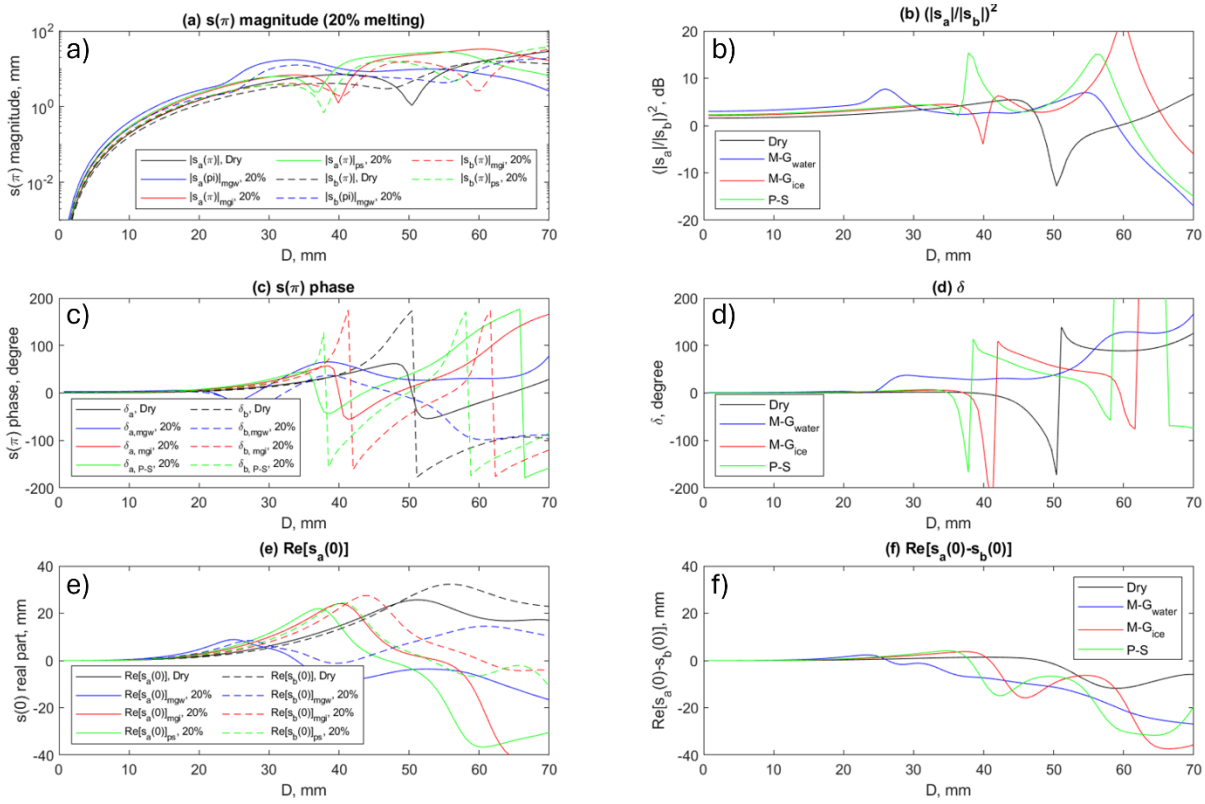


Figure 4: Scattering calculations using the T-matrix method for dry (black) hail and 20% melted hail with water as background (blue), ice as background, and both as inclusions (green): (a) absolute value of backscattering magnitude as a function of diameter for both horizontal (solid) and vertical (dashed) axis. (b) squared ratio of horizontal and vertical absolute scattering magnitude. (c) backscattering phase for both horizontal and vertical axis. (d) differential backscattering phase (δ_a - δ_b). (e) real parts of forward scattering amplitudes for horizontal and vertical axis. (f) difference in real parts of the forward scattering amplitudes.

Figure 4a and Figure 5a illustrate the absolute value of the scattering amplitude. Since the square of this amplitude is proportional to the scattering cross section, it directly influences the radar reflectivity factor (Z_h or Z_v). In the initial regime, all tests exhibit a monotonic increase in scattering amplitude, consistent with Rayleigh scattering, where particles are much smaller than the radar wavelength. However, as the hydrometeor size surpasses the Rayleigh scattering limit, resonance effects become apparent. These effects manifest at smaller diameters when the melting percentage is higher, likely due to an increased effective dielectric constant (ε_e). This is expected, as the presence of liquid water, which has a significantly higher dielectric constant than ice, enhances the scattering efficiency even at smaller diameters.

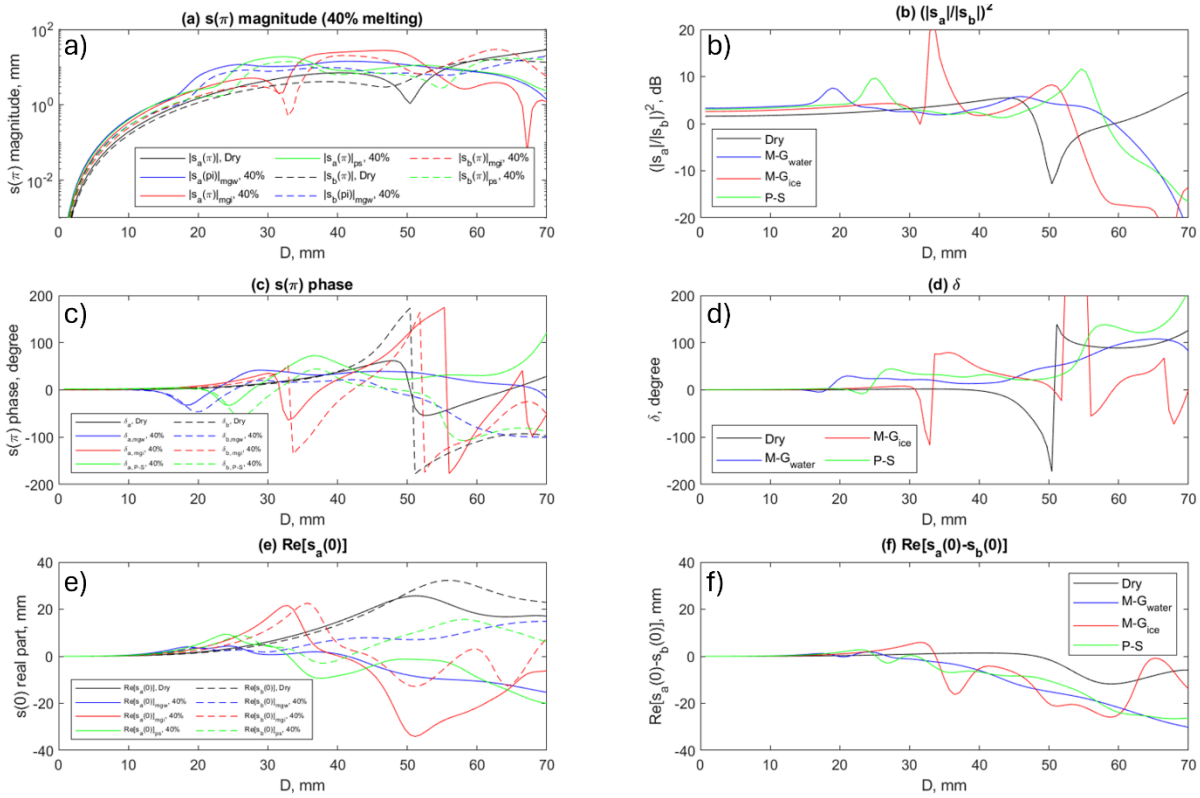


Figure 5: Same as Figure 4 but with 40% melting.

Figure 4b and Figure 5b present the squared magnitude of the ratio of scattering amplitudes in decibels between the major and minor axis polarizations, corresponding to the differential

reflectivity (Z_{DR}) for monodisperse hailstones. All test cases exhibit a similar initial trend: Z_{DR} increases monotonically, remains positive until a local maximum is reached, and then begins to decline. The location of this local maximum in Z_{DR} is strongly dependent on the effective dielectric constant. For 'dry' hailstones, the maximum occurs at a diameter of approximately 45 mm. In contrast, for the Maxwell-Garnett (M-G) test case with 40% melting and water as the background medium, the maximum is reached at a much smaller diameter of ~19 mm. This shift is consistent with the fact that a higher water fraction causes resonance effects to emerge at smaller sizes.

As the influence of water on ε_e decreases—whether by reducing the melting percentage, using ice as the background medium, or treating both ice and water as inclusions—the monotonic increase in Z_{DR} extends to progressively larger diameters before resonance effects become dominant. In all cases, once the maximum Z_{DR} is reached, resonance effects introduce oscillatory behavior, and negative values may appear. The Z_{DR} profile of the 'dry' hail case, as shown in Figure 4b, closely aligns with the findings of Seliga and Bringi (1978). Furthermore, similar resonance-driven variations in polarimetric scattering have been observed in radar measurements of tornado debris, highlighting the broader implications of these effects in real-world observations.

Figure 4c and Figure 5c illustrate the phase of the backscattered waves polarized along the major and minor axes for hailstones of varying sizes and dielectric properties. The phase evolution follows distinct regimes as the particle size increases, transitioning from Rayleigh scattering to resonance effects. For small hailstones, where the particle diameter is much smaller than the radar wavelength, the phase remains relatively stable with only a small difference

between the major and minor axis polarizations. This is expected, as Rayleigh scattering leads to a nearly uniform phase response with minimal differential phase shift.

As the hailstone size increases beyond the Rayleigh regime, resonance effects begin to emerge, introducing oscillations in the phase. The onset and severity of these oscillations depend strongly on the effective dielectric constant (ε_e). In the M-G model with 40% melting and water as the background medium, the phase remains near zero until the hailstone reaches approximately 12 mm in diameter, at which point a sharp decrease in phase is observed for both polarizations. In contrast, for the 'dry' hail case, the initial increase in phase is gradual and extends up to ~48 mm, with significantly higher phase values—particularly for the minor axis polarization. These two cases represent the extremes in terms of water content and its effect on ε_e, and all other test cases exhibit intermediate behavior, with the first local maximum occurring between ~20 mm and 50 mm.

A higher melting percentage corresponds to a higher effective dielectric constant (ε_e), which accelerates the onset of scattering phases. This results in resonance effects appearing at smaller diameters compared to the dry hail case. Consequently, in the M-G 40% melting case, strong oscillations occur much earlier than in the dry hail scenario, where the phase continues to increase over a much broader size range before experiencing oscillatory behavior. Regardless of the test case, once the phase reaches its initial maximum, resonance effects become dominant, leading to a decrease in phase followed by oscillatory fluctuations. Additionally, the abrupt, nearly asymptotic decreases observed in some profiles—most notably for the minor axis polarization—are the result of phase folding, where the phase wraps around due to periodicity.

Figure 4d and Figure 5d present the differential backscattering phase (δ), which is the backscattering phase difference between the waves polarized along the major and minor axes.

Balakrishnan and Zrnic (1990) used T-matrix calculations with an aspect ratio of 0.8 and showed that spongy hail (40% water) could produce substantial variations in δ beyond 5 cm, displaying values ranging from −50° to 90°. In contrast, dry hail exhibited only minor phase differences, with δ reaching about 8° at 8 mm, then decreasing to −20° at 50 mm. Our simulations show similar trends, though the exact values differ—likely due to variations in aspect ratio, dielectric constant estimation, or melting model assumptions.

From Figure 5d, we see that δ is non-negligible for hailstones larger than ~10 mm. In the 40% melting simulations, where water has a more substantial impact on the effective dielectric constant (ε_e), the onset of negative δ occurs at smaller diameters. For instance, in the $M{-}G_{\text{water}}$ and melting P-S cases, δ becomes negative around 15 mm (~22 mm for P-S). However, resonance effects soon reverse this trend, steering δ toward positive values. At 20 mm, $M{-}G_{\text{water}}$ exhibits $\delta \approx 30°$, while P-S reaches 40° at 25 mm. Similarly, Figure 4d shows that for 20% melting ($M{-}G_{\text{water}}$), δ reaches ~40° at 28 mm, demonstrating that increased water content accelerates the onset of phase oscillations. After reaching these initial maxima, the resonance effects cause a temporary dip, followed by a subsequent increase in δ. This behavior is characteristic of the transition from Rayleigh to non-Rayleigh scattering, where interference effects become prominent.

For cases where the influence of water on ε_e is minimized (e.g., ice-background, dry hail, and 20% P-S cases), the δ profile differs notably. In these cases, a small initial increase in δ is observed in the Rayleigh regime before transitioning to negative values at larger diameters. The diameter at which δ turns negative increases as the water influence on ε_e decreases. $M{-}G_{\text{ice}}$ at 40% melting (Figure 5d) exhibits a sharp decrease in δ starting around 30 mm. For dry hail, this downward shift is delayed until ~45 mm, emphasizing the role of water in shifting the onset of

resonance effects. While phase folding complicates the interpretation of δ at higher diameters, we want to highlight that at larger diameters, resonance effects allow δ to fluctuate between positive and negative values, reflecting the complex phase interactions in the non-Rayleigh scattering regime.

Figure 4e and Figure 5e depict the real parts of the forward scattering amplitudes for both the major and minor axes, which directly influence the specific propagation phase due to hydrometeors. Recall from Eq. (2.10) that specific differential phase (K_{DP}) is approximately given by the integral of the difference between these real parts, weighted by the drop size distribution (DSD) and canting angle parameters. The standard deviations of the canting angles in both the scattering plane (σ_ϑ) and the polarization plane (σ_φ) also contribute to this integral, influencing K_{DP} behavior.

Figure 4f and Figure 5f present the difference between the real parts of the forward scattering amplitudes at the major and minor axes. Initially, we observe a steady increase in this difference, consistent with the Rayleigh scattering regime, where scattering remains predictable and K_{DP} follows an approximately monotonic trend. However, once resonance effects emerge, the difference exhibits oscillations, including the appearance of negative values.

Among all tested cases, the 40% $M{-}G_{ice}$ scenario shows the largest peak difference ($\sim 6\ mm$), while no other case exceeds ~4.5 mm. Notably, in the 40% $M{-}G_{water}$ case, negative values appear at diameters as small as 19 mm, whereas in dry hail, which maintains positive values over a broader size range, negative values do not emerge until approximately 50 mm.

Because K_{DP} is proportional to the difference of real parts of the forward scattering amplitudes as shown in (2.13), these results highlight a key insight: K_{DP} does not behave as a strictly monotonic function beyond the Rayleigh regime. This challenges common operational

assumptions, particularly in radar data interpretation. For example, negative K_{DP} is often attributed to vertically oriented particles due to charge differentials in elevation. However, these results suggest that large particles undergoing resonance scattering can also introduce negative K_{DP}, independent of charge effects and the vertical alignment.

This observation underscores the complexity of interpreting K_{DP} in operational settings. In addition to known factors such as δ (differential backscattering phase) and measurement error (ε), non-Rayleigh scattering from large, irregular hydrometeors can also produce negative K_{DP} values. Furthermore, non-uniform beam filling (Ryzhkov and Zrnić 1998) can contribute to these negative values, particularly in regions such as the melting layer. This is especially relevant when considering linear least squares fitting (LSF) methods used in radar retrievals: when applied to non-monotonic phase profiles ($\widehat{\Phi}_{DP}$), these techniques can induce negative K_{DP} artifacts at the trailing edge of a localized phase bump. Thus, Figure 4f and Figure 5f reinforce that negative K_{DP} should not always be interpreted solely as a signature of vertically aligned particles but may also arise from large, melting or partially melted hydrometeors where resonance scattering effects dominate.

2.3 Non-Uniform Beam Filling

Per equations (4.86 & 4.143) of Zhang (2016), the differential phase is the phase of the cross-correlation function:

$$\langle n s_a^* s_b \rangle = \langle n | s_a | | s_b | \rangle e^{-\frac{\sigma_\delta^2}{2}} e^{j\delta} e^{j\phi_{DP}} \tag{2.18}$$

When non-uniform beam filling occurs, it is the volume averaged value, which can be expressed as follows:

$$\overline{\langle n s_a^* s_b \rangle} \approx \overline{\langle n | s_a | | s_b | \rangle} e^{-\frac{\sigma_\delta^2}{2}} e^{j\delta} e^{-\frac{\sigma_{\phi_{DP}}^2}{2}} e^{j\phi_{DP}} \tag{2.19}$$

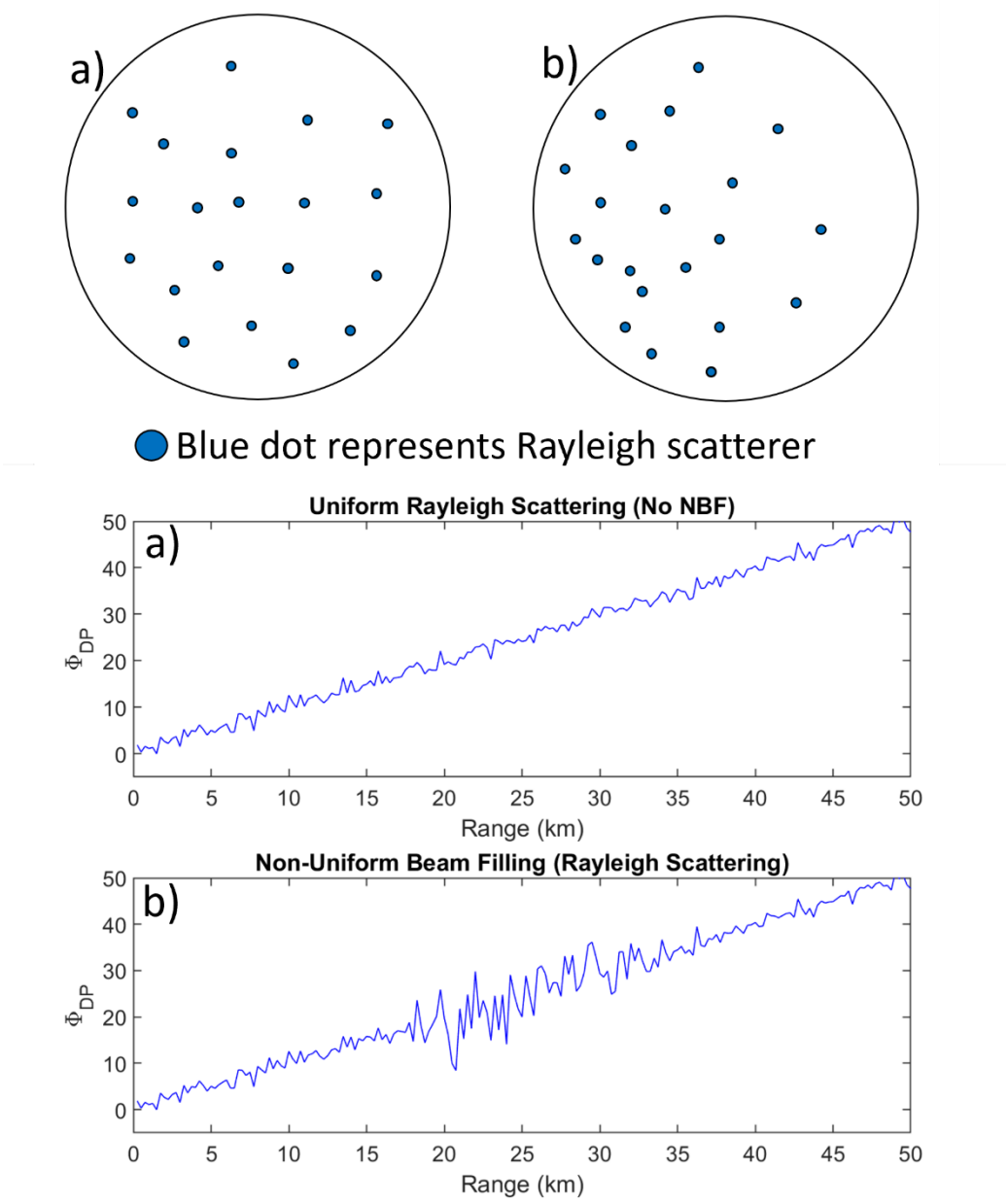


Figure 6: Illustration of radar beam resolution volume and associated $\widehat{\Phi}_{\mathrm{DP}}$ profile for a) uniform beam filling of Rayleigh regime scatterers and b) non-uniform distribution of Rayleigh regime scatterers.

Figure 6 illustrates two beam resolution volumes and the associated $\widehat{\Phi}_{DP}$ for two cases of Rayleigh regime scatterers. In one case (Figure 6a) we show a case of homogenously distributed Rayleigh scatterers. The associated $\widehat{\Phi}_{DP}$ profile is, primarily monotonically increasing, with small random fluctuations which can be attributed to measurement error. In Figure 6b, we see an

uneven distribution of the Rayleigh scatterers. For this case, the variance in propagation across the beam will be contributed by $e^{-\frac{\sigma^2_{\phi_{DP}}}{2}}$ term, which will lead to more notable random fluctuation as seen in the 1D $\widehat{\phi}_{DP}$ profile shown in Figure 6b. Thus, when the resolution volume contains only Rayleigh scatterers, no matter if they are uniformly or non-uniformly distributed, will have no impact from δ. The case of NBF with only these Rayleigh regime scatterers will cause reduced ρ_{hv} and larger fluctuations from gate to gate in the $\widehat{\phi}_{DP}$ profile.

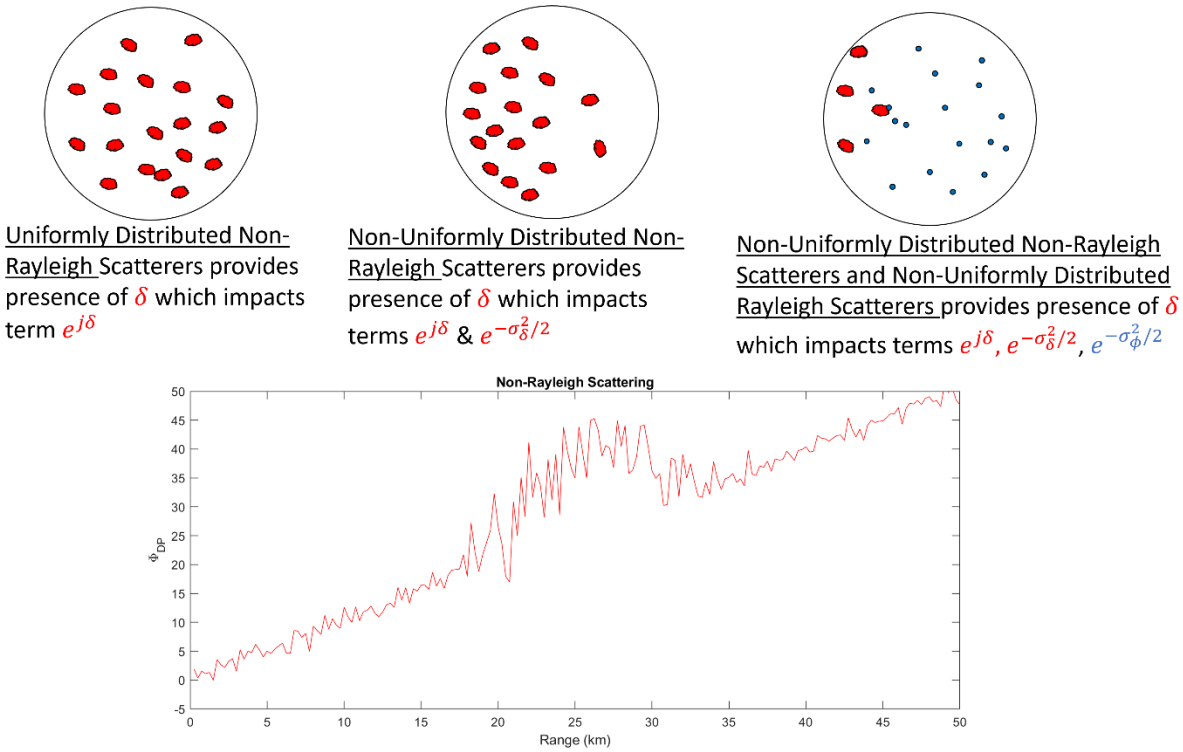


Figure 7: Illustration of radar beam resolution volumes containing different distributions of non-Rayleigh regime scatterers and an associated $\widehat{\phi}_{DP}$ profile displaying a uniform spatial feature associated with δ.

Figure 7 illustrates multiple examples of radar resolution volumes containing non-Rayleigh regime scatterers. It is the presence of these non-Rayleigh scatterers that provide the contribution of δ. The presence of δ can allow for the uniform spatial feature such as a 'bump 'or 'dip' in the $\widehat{\phi}_{DP}$ profile.

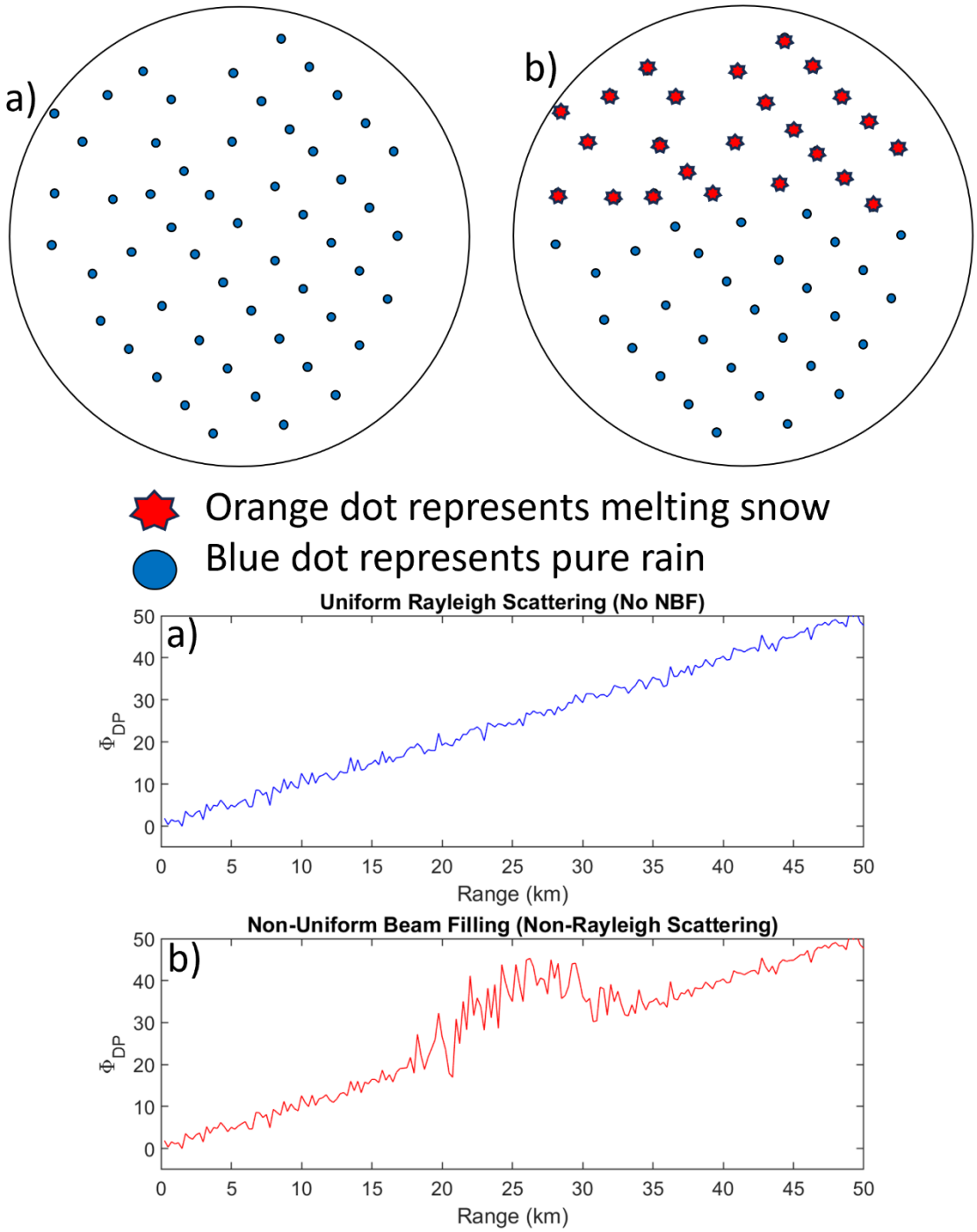


Figure 8: Illustration of radar beam resolution volumes and associated $\widehat{\Phi}_{DP}$ profiles for a) uniformly distributed Rayleigh regime scatterers and b) non-uniform distribution of Rayleigh and non-Rayleigh regime scatterers for a beam passing through the melting layer.

Finally, Figure 8 compares a resolution volume of a beam passing through pure rain against that of a beam passing through the melting layer. For the beam passing through melting snow and rain, that is what is often referred to as non-uniform beam filling. Because of the presence of the non-Rayleigh scatterers, we would expect this resolution volume to result in a spatial feature, such as a 'bump,' in the $\widehat{\Phi}_{DP}$ profile.

2.4 Complications with Estimating K_{DP}

The specific differential phase, K_{DP}, is defined in Eq. (2.11) and can be estimated using measurements of Φ_{DP} at two consecutive range gates:

$$\widehat{K}_{DP} = \frac{1}{2}\frac{\widehat{\Phi}_{DP}(r_2) - \widehat{\Phi}_{DP}(r_1)}{(r_2 - r_1)} \tag{2.20}$$

when $\widehat{\Phi}_{DP}$ is free of differential backscatter phase (δ) and devoid of measurement error (ε). However, due to statistical errors, directly obtaining a reliable K_{DP} estimate from Eq. (2.20) is often impractical. Since hydrometeor characteristics tend to remain relatively consistent over short distances, using multiple gates for estimation can improve accuracy.

To address this, operational radars typically employ Least Squares Fitting (LSF) to determine K_{DP} . This method estimates K_{DP} as the slope of ϕ_{DP} across multiple adjacent gates. The WSR-88D radar system applies a piecewise filtering approach based on reflectivity (Z_H) to select the appropriate filter length. Specifically, if Z_H at a given gate is 40 dBZ or below, a longer filter (25 gates, 6.25 km) is used; if Z_H exceeds 40 dBZ, a shorter filter (9 gates, 2.25 km) is applied. The LSF estimate of K_{DP} is given by (Doviak and Zrnić 1993):

$$\widehat{K}_{DP}(\bar{r}) = \frac{\sum_{i=1}^{n}\left[\left(\widehat{\Phi}_{DP}(i) - \bar{\widehat{\Phi}}_{DP}\right)\cdot(r(i) - \bar{r})\right]}{2\sum_{i=1}^{n}(r(i) - \bar{r})^2} \tag{2.21}$$

where $\bar{r}$ represents the mean range (i.e., the location of the intermediate gate), n is the filter length (9 or 25 gates), and $\overline{\widehat{\Phi}}_{DP}$ is the mean differential phase across the filter window. This technique effectively reduces error (ε) but does not eliminate artifacts from δ, which can still be present in $\widehat{\Phi}_{DP}$. This issue is illustrated in Figure 9, where an LSF-estimated differential propagation phase is applied to the measured $\widehat{\Phi}_{DP}$ profile shown in Figure 3. The LSF method effectively minimizes errors in the Rayleigh scattering regime (40-55 km). However, at non-Rayleigh scattering regions (55-80 km), where distinct "bumps" are visible in the $\widehat{\Phi}_{DP}$ profile, residual δ artifacts persist.

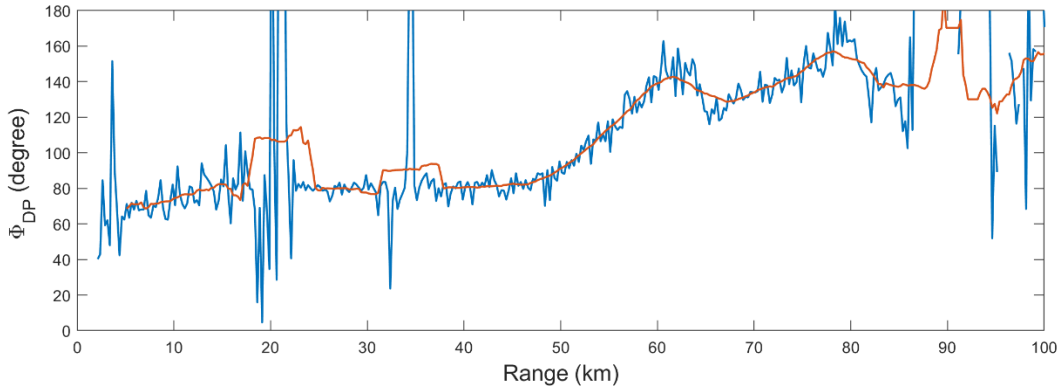


Figure 9: Measured radial profile of differential phase (blue) with LSF estimation of ϕ_{DP} (red line).

This limitation becomes particularly problematic when deriving K_{DP}. If we take the range derivative of the LSF-estimated ϕ_{DP} (Figure 9), the δ artifacts cause unphysical behavior: overestimated positive K_{DP} values on one side and large negative values on the other. As a result, hail cores and melting layers can produce extreme and unrealistic $\widehat{K}_{DP}$ values (Giangrande & Ryzhkov 2008), leading to erroneous calculations in rain rate estimates. To illustrate this, Figure 10 presents a supercell east of KTLX on May 4, 2022.

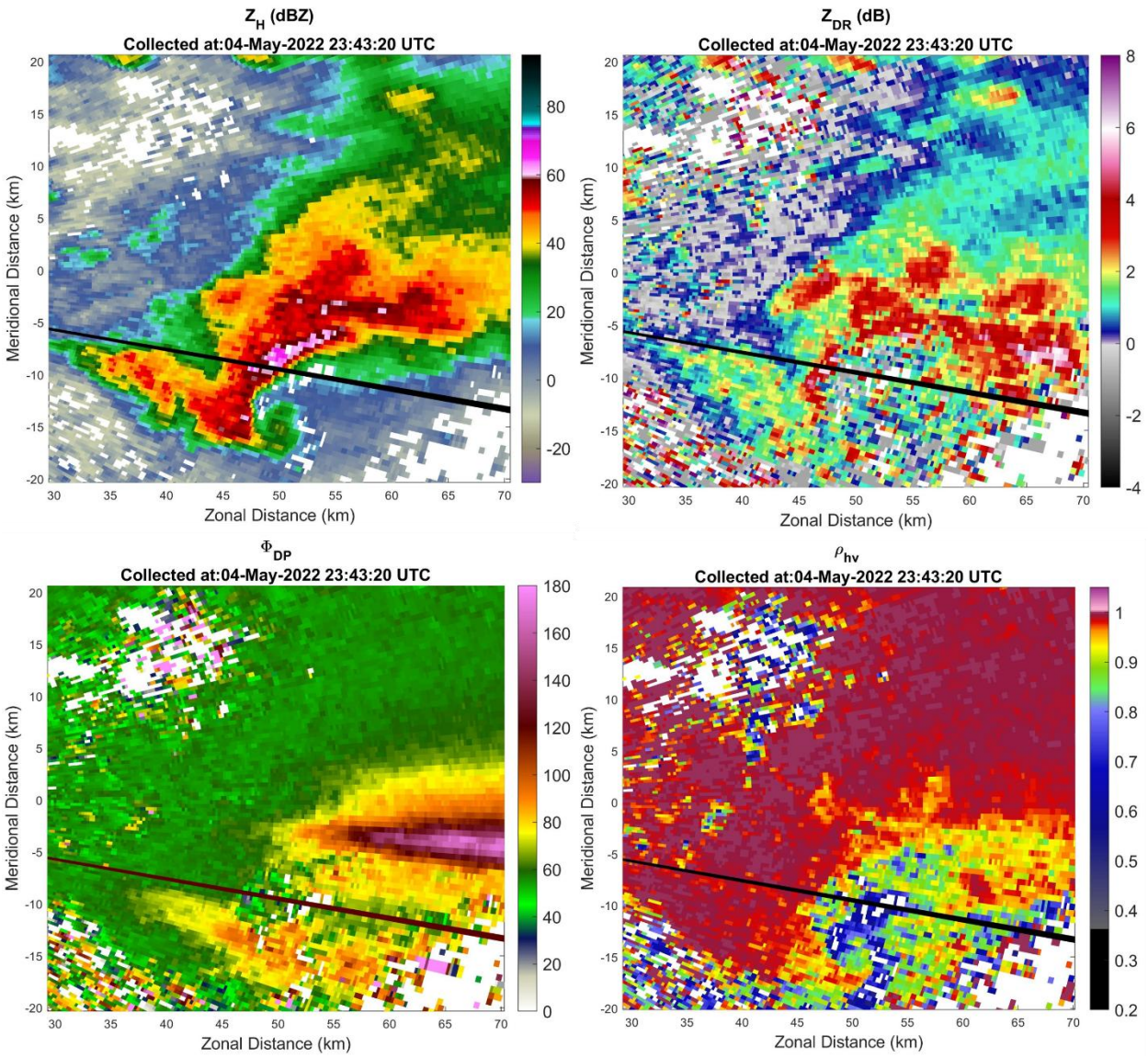


Figure 10: Low-elevation (0.5°) surveillance mode raw data from KTLX at 2343 UTC on May 04, 2022 of (top left) reflectivity factor (Z_H), (top right) differential reflectivity (Z_{DR}), (bottom left) total differential phase ($\widehat{\phi}_{DP}$), and (bottom right) co-polar correlation coefficient (ρ_{hv}). The shaded ray illustrates the 1D radial analyzed in Figure 11.

A specific radar radial passing through the hail core has been highlighted. The corresponding 1D radial profile (Figure 11) shows a reflectivity peak (Z_H > 55 dBZ, ~46-51 km), along with a collocated drop in ρ_{hv} and Z_{DR} (Figure 10). These signatures strongly indicate hail contamination.

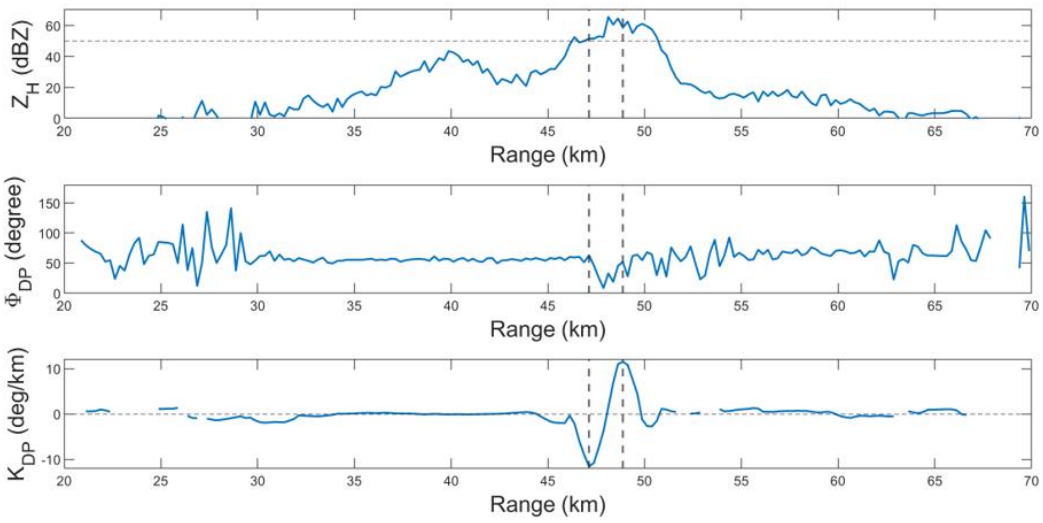


Figure 11: Illustrates the 1D radial profile of reflectivity (Z_H), $\widehat{\Phi}_{DP}$, and LSF estimated K_{DP} for the shaded ray in Figure 10.

Within the peak reflectivity region (46-49 km, dashed lines), the LSF-estimated ϕ_{DP} profile exhibits a uniform dip, which propagates into the LSF-estimated K_{DP} values, producing oscillations of approximately $\pm 11° \, km^{-1}$. Applying a standard power-law rain rate relation (Giangrande and Ryzhkov 2008),

$$R(K_{DP}) = 44|K_{DP}|^{0.822} sign\,(K_{DP}) \tag{2.22}$$

yields unrealistic rain rates of $\pm 315 \, mm \, hr^{-1}$, further demonstrating the pitfalls of neglecting δ in K_{DP} estimation.

To mitigate the impact of non-Rayleigh scattering regimes, previous research has developed alternative estimation techniques. Giangrande et al. (2013) introduced a linear programming (LP) approach, which applies monotonic constraints to ϕ_{DP} and ensures non-negative K_{DP} values. This method reduces the mean bias error of $\widehat{K}_{DP}$ from $0.18° \, km^{-1}$ (LSF) to $° \, km^{-1}$ (Giangrande et al. 2013). Building upon this, Huang et al. (2016) incorporated upper and lower bounds for $\widehat{K}_{DP}$ using self-consistent relationships between Z_H, Z_{DR}, and ϕ_{DP}. These constraints were integrated into the

LP framework to refine the estimation process. However, despite these advancements, no approach has yet successfully estimated or directly accounted for δ.

The methodology in this study combines classification and fitting techniques to improve K_{DP} estimation. Rather than applying a single fitting method across the entire profile, we first classify each radar gate as belonging to either a Rayleigh or non-Rayleigh scattering regime using measurements of ϕ_{DP}, Z_{H}, and ρ_{hv}. The LP approach is then applied exclusively within Rayleigh-classified regions, allowing for accurate K_{DP} estimates. These estimates are subsequently interpolated into adjacent non-Rayleigh regions, enabling the retrieval of δ. This composite approach aims to enhance the robustness of $\widehat{K}_{\mathrm{DP}}$ retrievals while mitigating influence from non-Rayleigh scattering. By incorporating classification into the estimation process, we seek to refine K_{DP}-dependent calculations, particularly those affecting rain rate estimation.

3. Data

This study utilizes Level II radar data from the 0.5° plan position indicator (PPI) scan to evaluate the proposed methodology while minimizing contamination from melting-layer effects. The selected cases include one confirmed hail event with a well-defined δ signature and two tornado cases exhibiting positive and negative δ signatures. These cases highlight how resonance effects can produce a broad range of δ values and hence cause substantial errors in the operationally used LSF K_{DP} estimation.

The radar observations were collected from the S-band KTLX and KDGX Weather Surveillance Radar-1988 Doppler (WSR-88D, also known as NEXRAD) systems, which have a beamwidth of 0.95° and a range resolution of 250 m. In addition to spatial and temporal resolution differences, radar observations are subject to various sources of contamination, including hail,

ground clutter, and anomalous propagation (Ulbrich and Lee 1999; Hubbert et al. 2009; Grams et al. 2019; Zhang et al. 2020). The impact of these factors on polarimetric variables is often understated, as commonly cited measurement sampling errors (e.g., $\Delta Z_{\mathrm{H}} \sim 1\ dbZ, \Delta Z_{\mathrm{DR}} \sim 0.2\ dB, \Delta\phi_{\mathrm{DP}} \sim 3°, \Delta\rho_{hv} \sim 0.006$) are primarily valid for rain-dominated regions where ρ_{hv} approaches 0.99 (Zhang 2016; Zhang et al. 2021). In contrast, when non-Rayleigh scattering is present, these errors for polarimetric variables ($Z_{\mathrm{DR}}, \phi_{\mathrm{DP}}, \rho_{hv}$) can be substantially higher. A single-ray profile comparison, such as in Figure 2, effectively illustrates the difference between measurement fluctuations in Rayleigh-scattering regions and the more pronounced systematic shifts that arise in non-Rayleigh scattering conditions.

While polarimetric radar measurements provide valuable insight into hydrometeor characteristics, they are inherently subject to measurement uncertainties. The total measured differential phase $\widehat{\phi}_{DP}$ consists of the propagation phase component, differential backscattering phase, and additional sources of error. As illustrated in Figure 2, within Rayleigh-scattering regions, the estimated ϕ_{DP} and measured $\widehat{\phi}_{DP}$ profiles closely align, with small oscillations around a common center. These fluctuations, denoted as ε, represent measurement error. However, in non-Rayleigh scattering regimes, a systematic offset between the estimated and measured $\widehat{\phi}_{DP}$ emerges, indicative of δ, the differential backscattering phase component. This bias is highly dependent on intrinsic properties such as δ itself, with larger fluctuation of the backscattering phase difference leading to reduced ρ_{hv}, which ultimately leads to greater errors in dual-polarization variables.

By incorporating these considerations, this study not only improves estimation but also enhances our understanding of how resonance effects impact radar observations, emphasizing the need for tailored error assessments in different scattering regimes.

4. Methods

This section outlines the procedure for estimating ϕ_{DP}, K_{DP}, and δ as first described in Mishler et al. (2024). The process begins by identifying and separating segments of Rayleigh scattering from non-Rayleigh scattering regimes. Once these regions are distinguished, an estimation of ϕ_{DP} and K_{DP} is performed within each Rayleigh scattering segment using linear programming. Along a given radial, these Rayleigh scattering segments are then connected to provide an estimation of ϕ_{DP} and K_{DP} in non-Rayleigh scattering regions. To improve visualization, the resulting estimates of ϕ_{DP} and K_{DP} are subsequently smoothed. Finally, δ is obtained by computing the difference between the measured differential phase shift, $\widehat{\Phi}_{\mathrm{DP}}$, and the estimated ϕ_{DP}. These steps are illustrated in the flow diagram shown in Figure 12.

The estimation process begins by determining an initial ϕ_{DP} value for each radial, as depicted in Figure 12a. For every radial, the first 15 range gates are examined. Any gate where ρ_{hv} is less than 0.96, or where both the reflectivity factor Z_H is below 0 dBZ and the signal-to-noise ratio (SNR) is below 20 dB, is excluded from consideration. From the remaining gates, a median value is calculated for each azimuth angle, producing one representative median per angle. Once these median values are obtained across all azimuth angles, a final median is computed to establish the starting ϕ_{DP} value. This initial value serves as the lower bound constraint in the linear programming function and is applied to all gates preceding the first Rayleigh scattering segment within each radial.

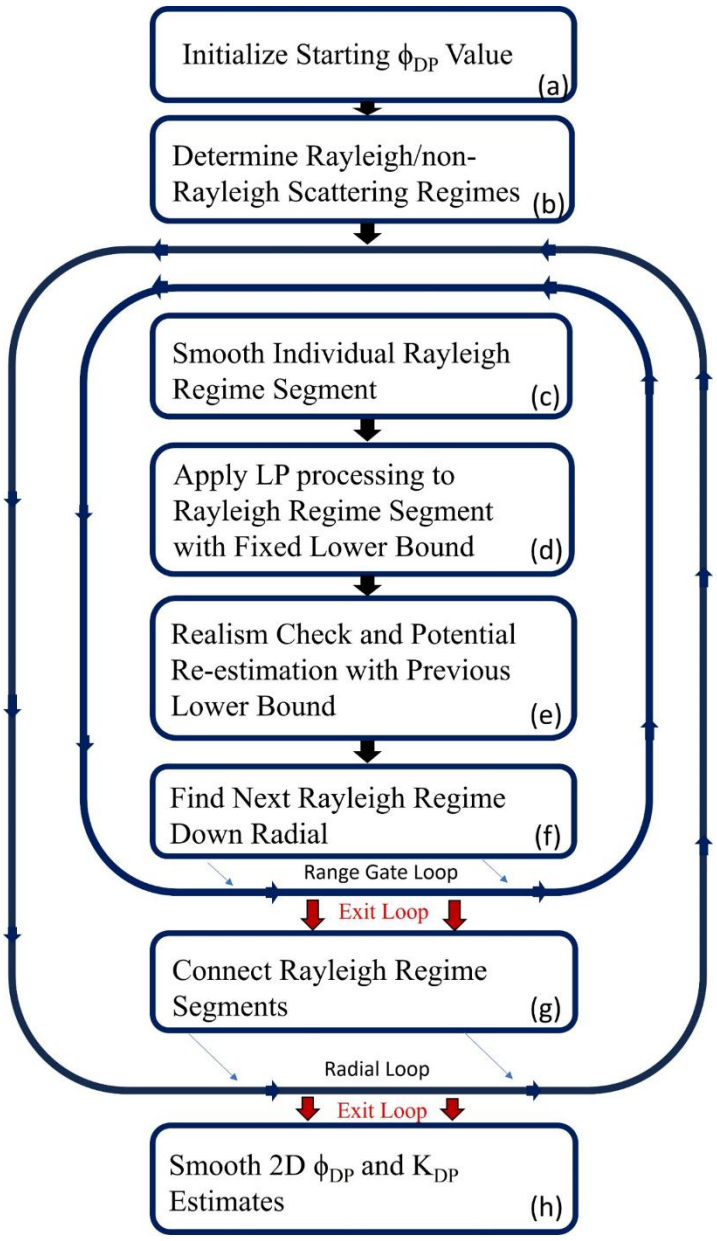


Figure 12: flow diagram illustrating the process used for estimating the differential propagation phase (ϕ_{DP}) and specific differential phase (K_{DP}) at a given elevation of a NEXRAD Level II data file. The range gate loop indicates traversing down range of a given radial while the radial loop indicates looping over radials at all azimuth angles.

Since the estimation of ϕ_{DP} must be performed within Rayleigh scattering regimes, it is first necessary to identify the gates where these regimes exist before proceeding with the estimation process. This step, illustrated in Figure 12b, is accomplished using a 5-point sliding window that

moves along each radial while analyzing the measured Z_H, Z_{DR}, ρ_{hv}, and $\widehat{\phi}_{DP}$. Due to the increased likelihood of clutter contamination near the radar, stricter criteria are applied within the first 11 km. In this region, all five gates within the sliding window must satisfy the following conditions to be classified as part of a Rayleigh scattering regime: ρ_{hv} must exceed 0.96, the signal-to-noise ratio (SNR) must be greater than 20 dB, and Z_H must be above 0 dBZ. Additionally, to ensure minimal variability in $\widehat{\phi}_{DP}$ across the window, its standard deviation must not exceed 6°. If all these criteria are met, the gates are flagged as 'good,' indicating that they belong to a Rayleigh scattering regime.

Beyond 11 km, slightly relaxed conditions are applied. The threshold for ρ_{hv} is lowered to 0.95, the SNR requirement is reduced to 5 dB, and a single gate within the 5-point window is permitted to deviate from these thresholds—meaning one gate may have either ρ_{hv}, SNR, or Z_H below the specified limits. These threshold values were selected based on the physical characteristics of Rayleigh scattering and their demonstrated ability to yield reliable results.

The estimation process begins by identifying the first Rayleigh scattering gate along a given radial using the previously established flags. From this point, we iterate through the 1D radial vector, as illustrated by the inner loop in Figure 12. If a 'bad' (non-Rayleigh) gate is encountered, the estimation window is immediately closed. If a NaN value appears in the measured $\widehat{\phi}_{DP}$, we mark its position and search forward for the next 'good' gate while keeping track of consecutive NaN occurrences. If either a 'bad' gate is detected or three or more consecutive NaN values appear, the estimation window is fixed from its starting position up to the gate just before the NaN sequence or the non-Rayleigh regime gate. Since NaN values may still exist within the estimation window, a 3-point median filter is applied to remove them, as shown in Figure 12c. Once this filtering step is complete, linear programming (LP) is used to

estimate both ϕ_{DP} and K_{DP} for the segment vector (Figure 12d). The method follows the approach outlined in Giangrande et al. (2013), which applies a series of linear constraints to minimize the difference between the given $\widehat{\Phi}_{\mathrm{DP}}$ profile and the estimated ϕ_{DP}, while ensuring a monotonic constraint that guarantees a non-negative K_{DP} profile.

To enforce a monotonic increase along each radial, the final value of the estimated ϕ_{DP} window is set as the lower bound for the next estimation window further down the radial. The subsequent estimation begins at the next 'good' gate following the previous window, as depicted in Figure 12f. However, even with the defined thresholds for identifying Rayleigh scattering gates, there remains a possibility of misclassification. To mitigate the risk of an unrealistically high lower bound distorting the estimates for subsequent down-radial segments, additional safeguards are implemented (Figure 13). Specifically, we analyze the difference between the measured $\widehat{\Phi}_{\mathrm{DP}}$ at the first gate of a new estimation window and the current lower bound (i.e., the estimated propagation phase at the final gate of the previous window) to prevent any significant discontinuities that could propagate errors through the remaining radial segments.

Figure 13a illustrates a case in which a faulty estimate segment (circled in black) at approximately 47 km introduces an unrealistic lower bound for the subsequent Rayleigh scattering segment (boxed in red) at around 50 km. In this instance, the estimated ϕ_{DP} at the last gate of the faulty segment is nearly 40° higher than the measured $\widehat{\Phi}_{\mathrm{DP}}$ at the beginning of the final Rayleigh scattering regime. If this lower bound were used in the LP estimation, the monotonic increase constraint would force an artificially large estimate, as shown in Figure 13a. To correct this issue, the erroneous estimate (circled in black) is removed, and instead, the final segment is estimated using the lower bound from the most recent valid Rayleigh scattering segment up radial. Figure 13b demonstrates this adjustment, where the lower bound from the

upstream Rayleigh estimate at approximately 30 km (circled in black) is applied to the final segment (boxed in red). This correction results in a more realistic down-radial estimate, while the faulty region is now classified as non-Rayleigh and is excluded from the estimation process.

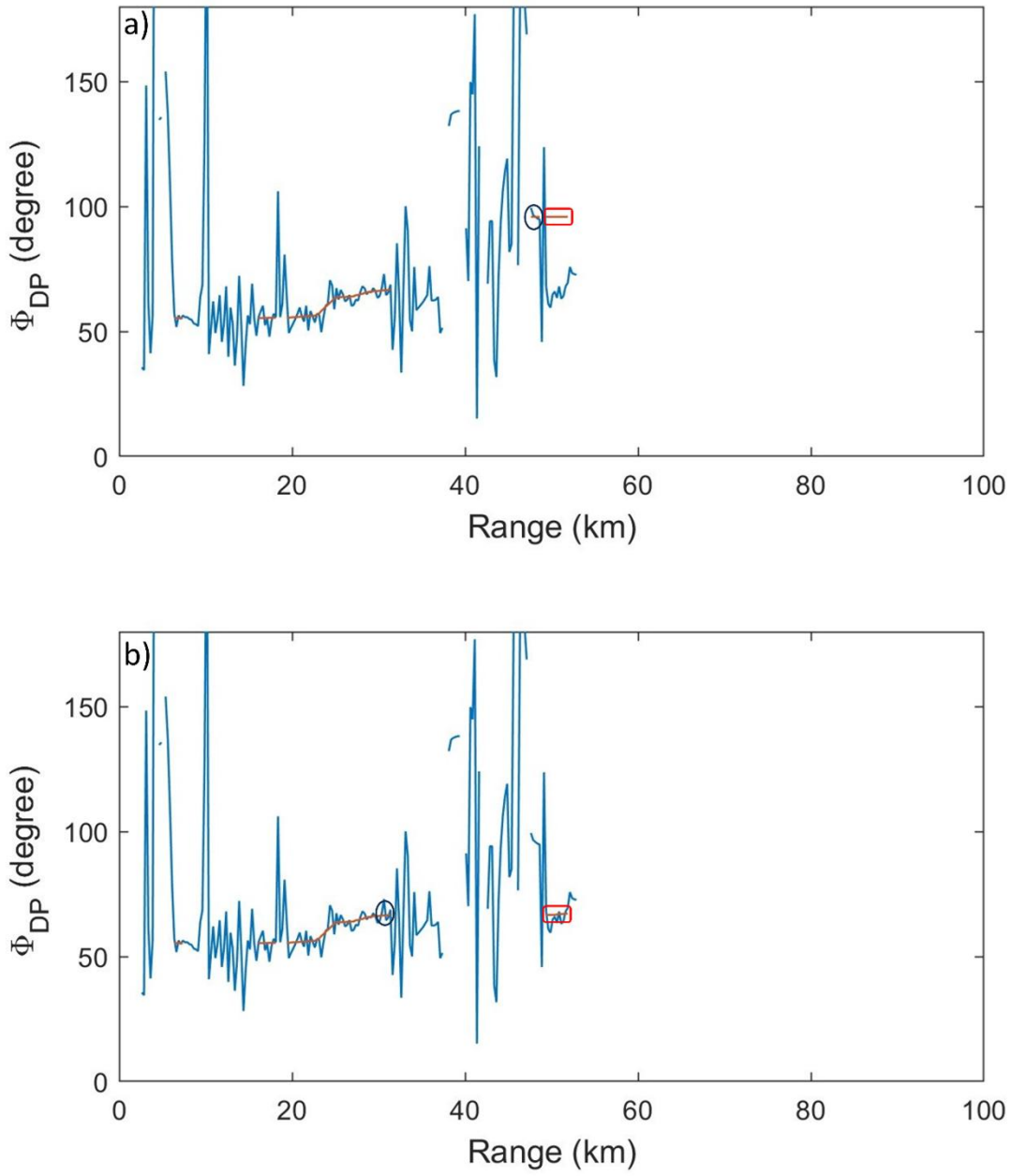


Figure 13: (a) illustrates how an incorrectly classified Rayleigh scattering estimate (circled) can result in a lower bound that causes a down-radial estimation (boxed in red) to be unrealistically high. (b) depicts the same radial estimation of ϕ_{DP} with the faulty segment removed such that the

later segment (boxed in red) would have been estimated with the lower bound provided by the previously estimated, up radial segment (circled in black).

Once the estimation process is completed for an entire radial, the next step is to connect the identified Rayleigh scattering segments, as illustrated in Figure 12g. To begin, all values in the estimate vector preceding the first Rayleigh regime gate are assigned the starting point value. The final gate of the first Rayleigh segment is designated as the left boundary, while the first gate of the subsequent Rayleigh segment serves as the right boundary. A linear interpolation is then applied between these boundaries to estimate ϕ_{DP} and K_{DP} within the non-Rayleigh scattering region. This interpolation process continues along the radial, ensuring that gaps between Rayleigh segments are bridged. Any non-Rayleigh scattering gate beyond the last identified Rayleigh segment is set to NaN in the ϕ_{DP} estimate vector. Figure 14 illustrates the outcome of this step for a single radial. In Figure 14a, the LP estimation of ϕ_{DP} is shown for each Rayleigh scattering segment. Figure 14b demonstrates how linear interpolation is used to fill in the non-Rayleigh scattering regions, providing a complete ϕ_{DP} estimate.

After interpolation, a smoothing step is applied to enhance the visualization of both estimates, as shown in Figure 12h. A 3-point median filter is used to smooth KDP azimuthally across radials. For the ϕ_{DP} estimate, each NaN gate is evaluated to determine whether its neighboring gates at the same range contain valid estimates. If so, linear interpolation is used to fill in missing values, followed by an azimuthal moving average with a 3-point sliding window to further smooth the field. Finally, with both ϕ_{DP} and K_{DP} fully estimated, the differential backscattering phase (δ) is calculated as the difference between the measured $\widehat{\Phi}_{\mathrm{DP}}$ and the estimated ϕ_{DP}.

We acknowledge that within non-Rayleigh scattering regions, the linear interpolation used to estimate ϕ_{DP} may deviate slightly from the true propagation phase, potentially impacting the accuracy of δ estimation. Additionally, the estimated δ may include some contributions from measurement errors. However, we believe this impact is relatively small, as differential backscattering phase typically remains on the order of 10°, suggesting that our estimation method should still provide reasonable accuracy within a few degrees. Furthermore, the assumption of a 'fixed' K_{DP} value within non-Rayleigh scattering regions likely differs from the true K_{DP}, which would naturally exhibit more variation. The intrinsic K_{DP} in these regimes depends on multiple poorly constrained factors, including particle size, shape, composition, and degree of melting. Given the lack of a widely accepted method for accurately determining these parameters, we opted for a linear interpolation approach for K_{DP} estimation in non-Rayleigh scattering regions. While this method provides a practical solution, future research may yield improved techniques for more precise retrievals.

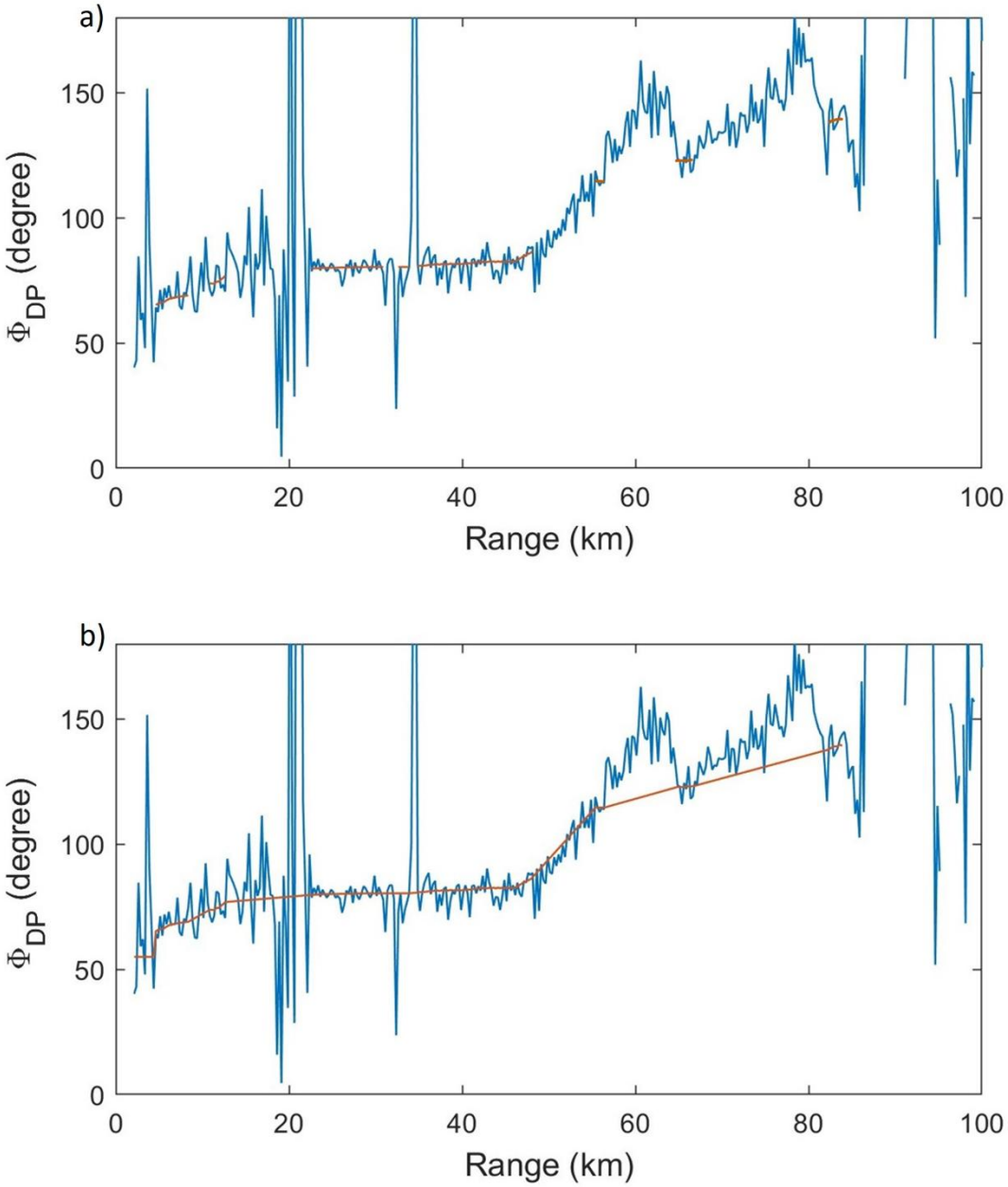


Figure 14: (a) illustrates $\widehat{\Phi}_{\mathrm{DP}}$ (blue) and the unconnected estimated ϕ_{DP} within the determined Rayleigh scattering regimes (red), (b) illustrates the same with linear interpolation used to connect the Rayleigh scattering regimes providing an estimation of ϕ_{DP} in non-Rayleigh scattering regimes.

5. Results

The methodology outlined in the previous section was applied to a case from April 19, 2023, when a 7.6 cm (3-inch) hailstone was reported in Amber, Oklahoma (SPC, 2023). For this analysis, we used level-II data from the WSR-88D KTLX radar (Oklahoma City, OK) at a low elevation angle (0.5°) from the 2330 UTC scan. These data files were sourced from Amazon Web Services (AWS, 2023). Additionally, we briefly examine two tornado cases where distinct δ signatures coincided with tornado debris signatures (TDSs), as discussed in prior studies (Ryzhkov et al. 2005b; Kumjian and Ryzhkov 2008). Specifically, we analyze the EF4 tornado that struck Rolling Fork, Mississippi, on April 24, 2023, and the EF3 tornado that impacted Cole, Oklahoma, on March 31, 2023.

Figure 15 provides a visualization of the supercell responsible for the 7.6 cm hailstone just minutes before the report from Amber, Oklahoma. The well-defined reflectivity (Z_H) structure of the storm, shown in Figure 15a, is located southwest of KTLX. Within the supercell's core, reflectivity values exceed 60 dBZ, suggesting the likely presence of large hail (circled in black). As discussed with regard to Figure 4b and Figure 5b, differential reflectivity (Z_{DR}) tends to drop below 0 dB when hailstones exceed the Rayleigh scattering regime. In Figure 15b, Z_{DR} values fall below 0 dB in the same region of high Z_H, further supporting the presence of hail. Additionally, Figure 15c shows that the cross-correlation coefficient (ρ_{hv}) drops below 0.9 in this area, reinforcing the hail signature. The total differential phase ($\widehat{\Phi}_{DP}$) in Figure 15d exhibits a significant increase near this hail core. Another region of enhanced reflectivity appears west-southwest of the primary supercell (boxed in black), also showing characteristics of a hail signature with Z_H values exceeding 55 dBZ, near-zero Z_{DR}, and low ρ_{hv} values (<0.9).

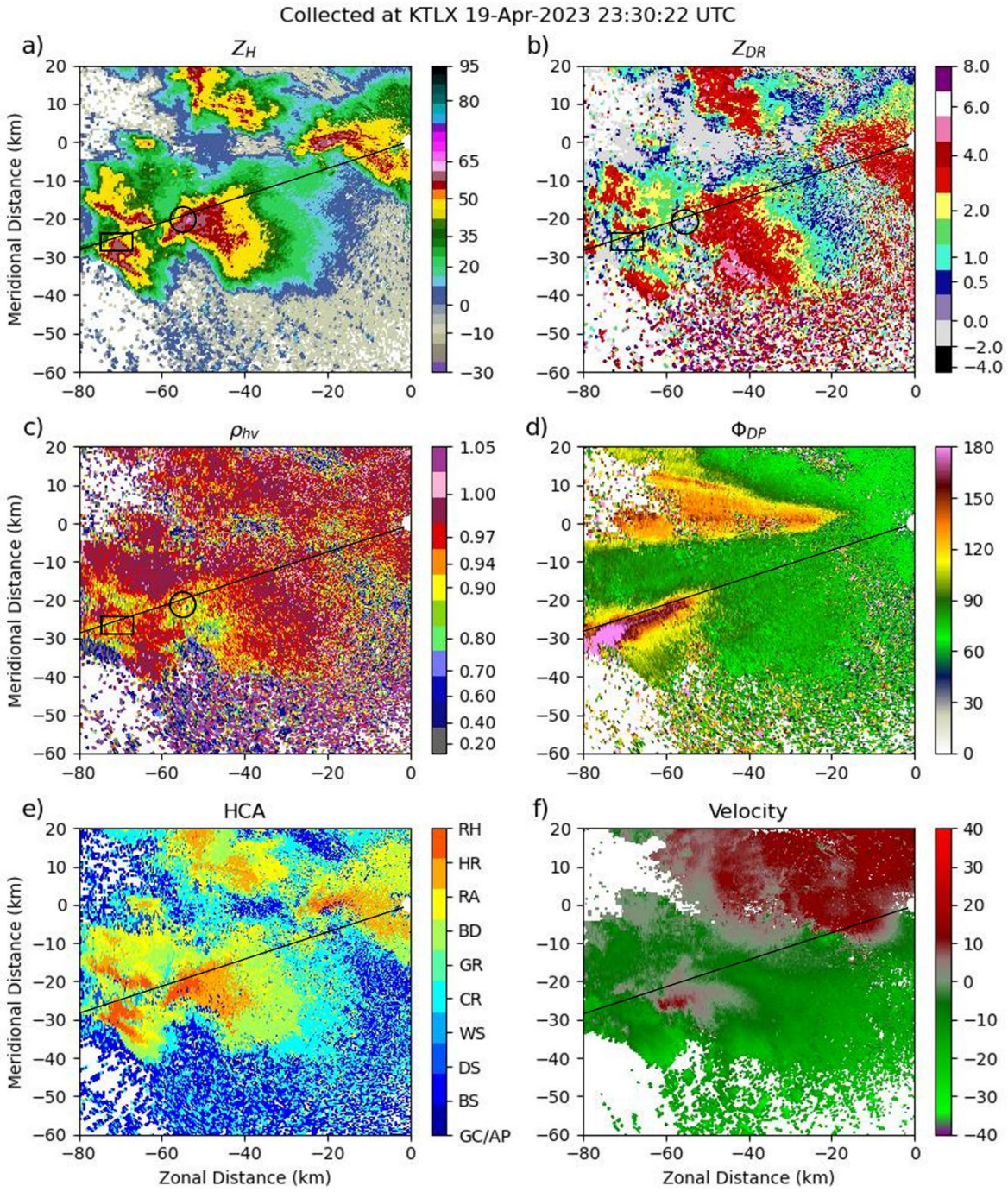


Figure 15: Low-elevation (0.5°) surveillance mode raw data from KTLX at 2330 UTC. (a) reflectivity factor (Z_H), (b) differential reflectivity (Z_{DR}), (c) co-polar correlation coefficient (ρ_{hv}), (d) total differential phase (ϕ_{DP}), (e) hydrometeor classification, and (f) radial velocity. The primary region of enhanced reflectivity is denoted with the black circle in plots a-c while the second region, farther down radial, is denoted with the black box.

To further investigate these hail signatures, we selected a single 1D radial for analysis, shown as the black ray in each panel of Figure 15. This ray extends through the north-northeastern periphery of both hail cores and was chosen to highlight evident 'bumps' in the $\widehat{\phi}_{DP}$ profile corresponding with positive δ. The corresponding 1D plots for this radial are shown in Figure 16. Between approximately 49 km and 60 km, Z_H remains above 50 dBZ, as indicated by the orange dashed lines in Figure 16c. Simultaneously, Z_{DR} decreases from around 5 dB at 50 km to a local minimum of approximately -0.5 dB at 57 km, consistent with the resonance effects shown in Figure 4b and Figure 5b.

The $\widehat{\phi}_{DP}$ profile remains relatively stable until around 50 km, after which it begins increasing. Notably, at 56 km, the slope of $\widehat{\phi}_{DP}$ steepens, reaching a local maximum at approximately 60 km before declining again around 65 km. This $\widehat{\phi}_{DP}$ peak occurs slightly downrange of the highest Z_H values, aligning with simulation results (Figure 4 and Figure 5) that suggest the maximum backscattering phase does not always coincide with the peak reflectivity. However, this $\widehat{\phi}_{DP}$ enhancement remains within the hail signature, as indicated by the trends in ρ_{hv} and Z_{DR}. A similar $\widehat{\phi}_{DP}$ pattern is observed between 75 km and 80 km, corresponding to the second region of enhanced reflectivity (between the vertical black dashed lines). Again, the local $\widehat{\phi}_{DP}$ maximum is slightly downrange of the highest Z_H values but remains aligned with low ρ_{hv} and Z_{DR}.

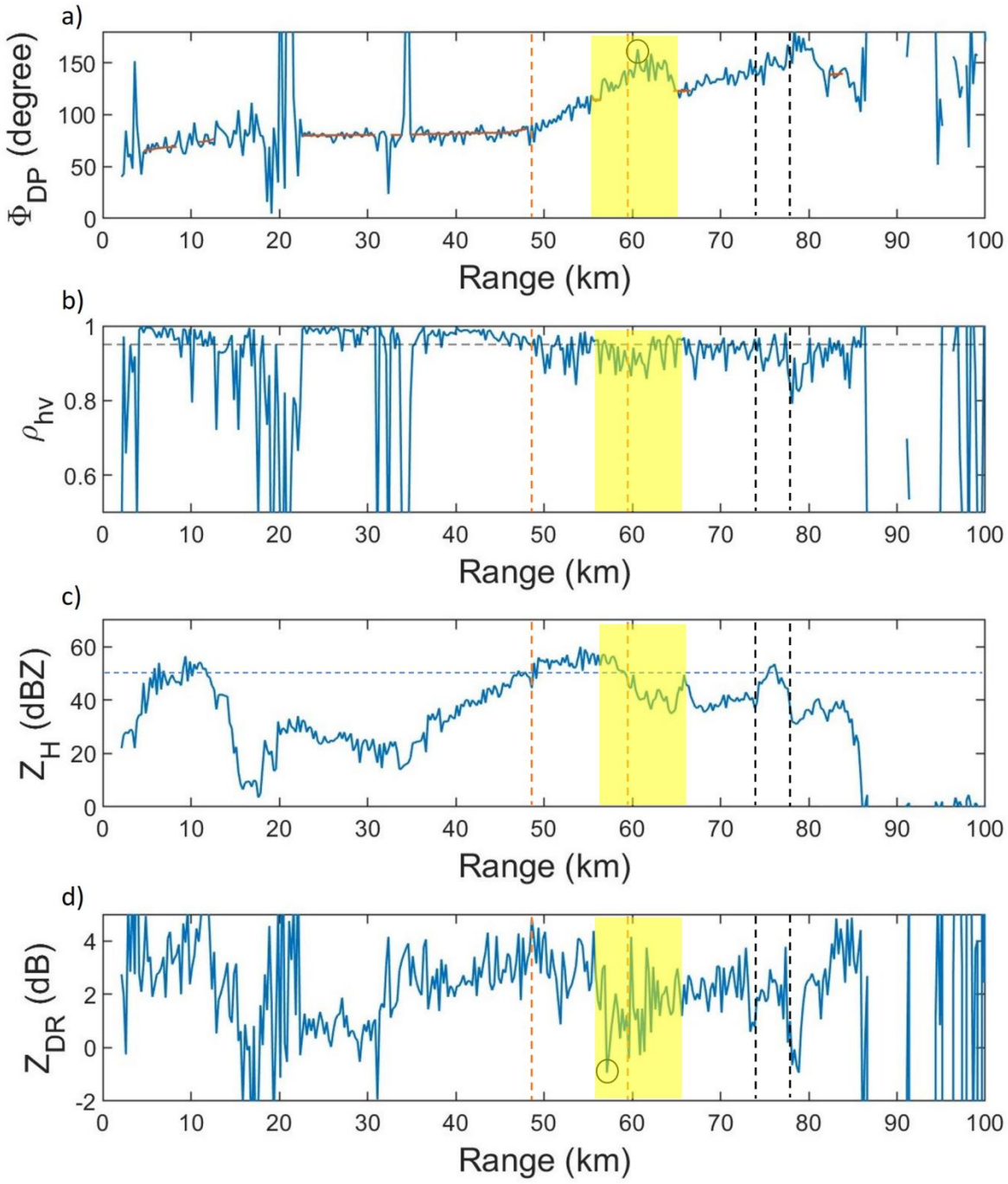


Figure 16: Ray plots of polarimetric radar data for the highlighted beam in Figure 15: (a) total differential phase ($\widehat{\Phi}_{DP}$), (b) copolar correlation coefficient (ρ_{hv}), (c) reflectivity factor (Z_H) with horizontal black line at 50 dBZ, and (d) differential reflectivity (Z_{DR}). The region between the vertical orange dashed lines indicate the first region of enhanced Z_H while the region between the

dashed black lines indicates the second region of enhanced Z_H. The yellow highlighted region depicts the region of the first 'bump' in $\widehat{\Phi}_{DP}$.

These results suggest that the $\widehat{\Phi}_{DP}$ bumps are likely caused by differential backscattering from hailstones exceeding the Rayleigh scattering regime. However, other factors such as differential attenuation and non-uniform beam filling may also contribute, particularly in the second $\widehat{\Phi}_{DP}$ peak, which coincides with Z_H values near 30 dBZ. The selected radial passes through regions with strong reflectivity gradients, often associated with significant hail. Beam broadening may allow hail to be captured within a radar side lobe, leading to reduced ρ_{hv} and altered $\widehat{\Phi}_{DP}$ values. In such cases of non-uniform beam filling, both Rayleigh and non-Rayleigh scattering can occur simultaneously. While the overall reflectivity may be dominated by the Rayleigh regime due to a higher number concentration of smaller particles, the presence of large hailstones within part of the beam resolution can still generate differential backscattering phase effects. Therefore, the observed $\widehat{\Phi}_{DP}$ enhancements are likely driven primarily by δ contributions from non-Rayleigh scatterers.

Figure 17 presents the 2D results demonstrating the effectiveness of the new methodology applied to the Amber, Oklahoma hail case. Figure 17a shows the estimated Φ_{DP}, which broadly captures the overall structure of the measured $\widehat{\Phi}_{DP}$ seen in Figure 15d. However, a key difference is the monotonic increase in ϕ_{DP} values, as the estimation is restricted to Rayleigh scattering regimes. At this low elevation angle (0.5°), the horizontally polarized wave is expected to be more influenced than the vertically polarized wave.

By subtracting the estimated ϕ_{DP} (Figure 17a) from the measured $\widehat{\Phi}_{DP}$ (Figure 15d), we obtain an estimate of δ, shown in Figure 17b. The hail region associated with the supercell exhibits positive δ signatures, particularly along the northern and southern edges of the hail core.

However, this signature diminishes near the center, likely due to resonance effects, as illustrated in Figure 4d and Figure 5d.

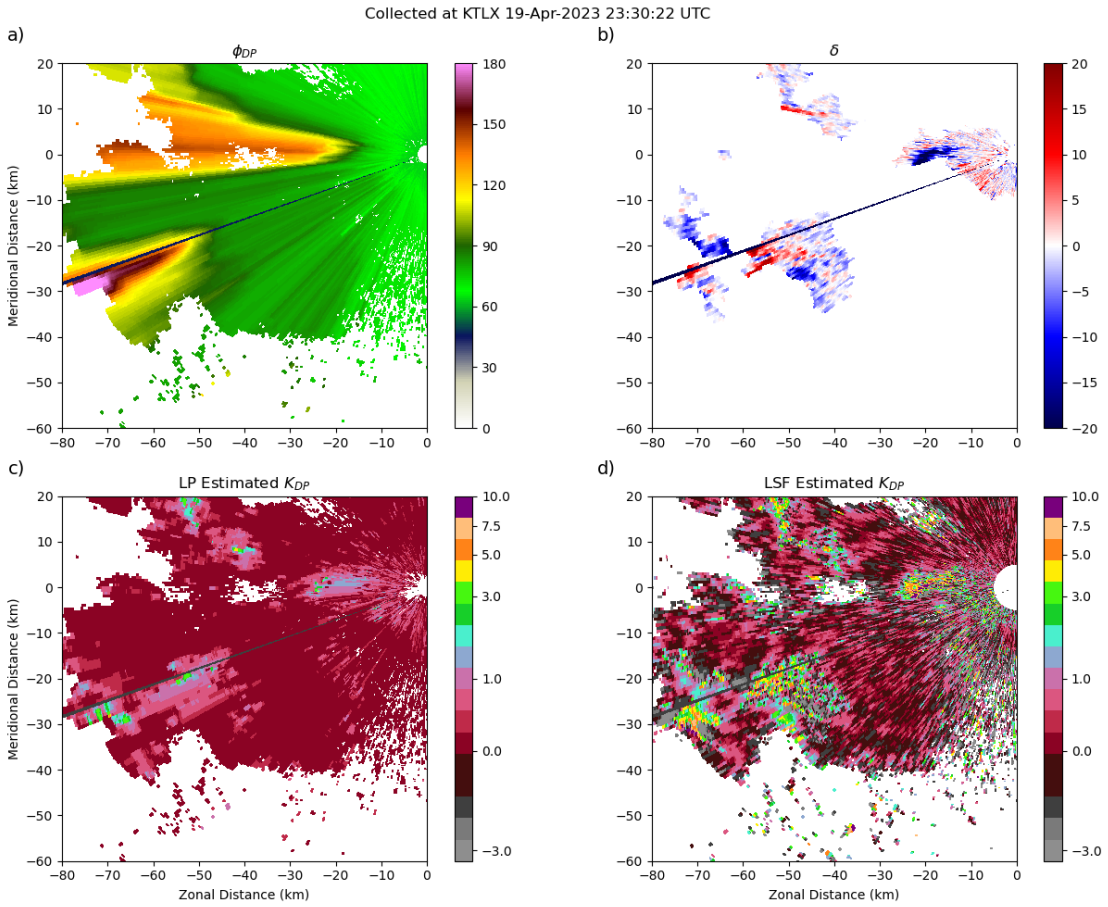


Figure 17: Estimation results for the image data shown in Figure 15: (a) estimated differential propagation phase ϕ_{DP}, (b) estimated differential backscattering phase δ, (c) LP estimated K_{DP}, and (d) LSF estimated K_{DP}.

Figure 17c and Figure 17d compare the estimated $\widehat{K}_{\mathrm{DP}}$ values obtained using two different methods: linear programming (LP) and least squares fit (LSF). The LSF approach (Figure 17d) produces noticeably larger positive $\widehat{K}_{\mathrm{DP}}$ values and also introduces negative estimates, which are physically inconsistent. This occurs because the LSF method applies a range derivative to the measured $\widehat{\Phi}_{\mathrm{DP}}$. As seen in Figure 16a, $\widehat{\Phi}_{\mathrm{DP}}$ can contain well-defined 'bumps' and the presence of these 'bumps' leads to artificially high $\widehat{K}_{\mathrm{DP}}$ values near the storm's leading edge, followed by

negative estimates near the trailing edge as seen in Figure 17d. In contrast, the LP method (Figure 17c) mitigates these issues by restricting calculations to Rayleigh scattering regimes. As a result, it produces significantly lower $\widehat{K}_{\mathrm{DP}}$ values and eliminates nonphysical negative estimates.

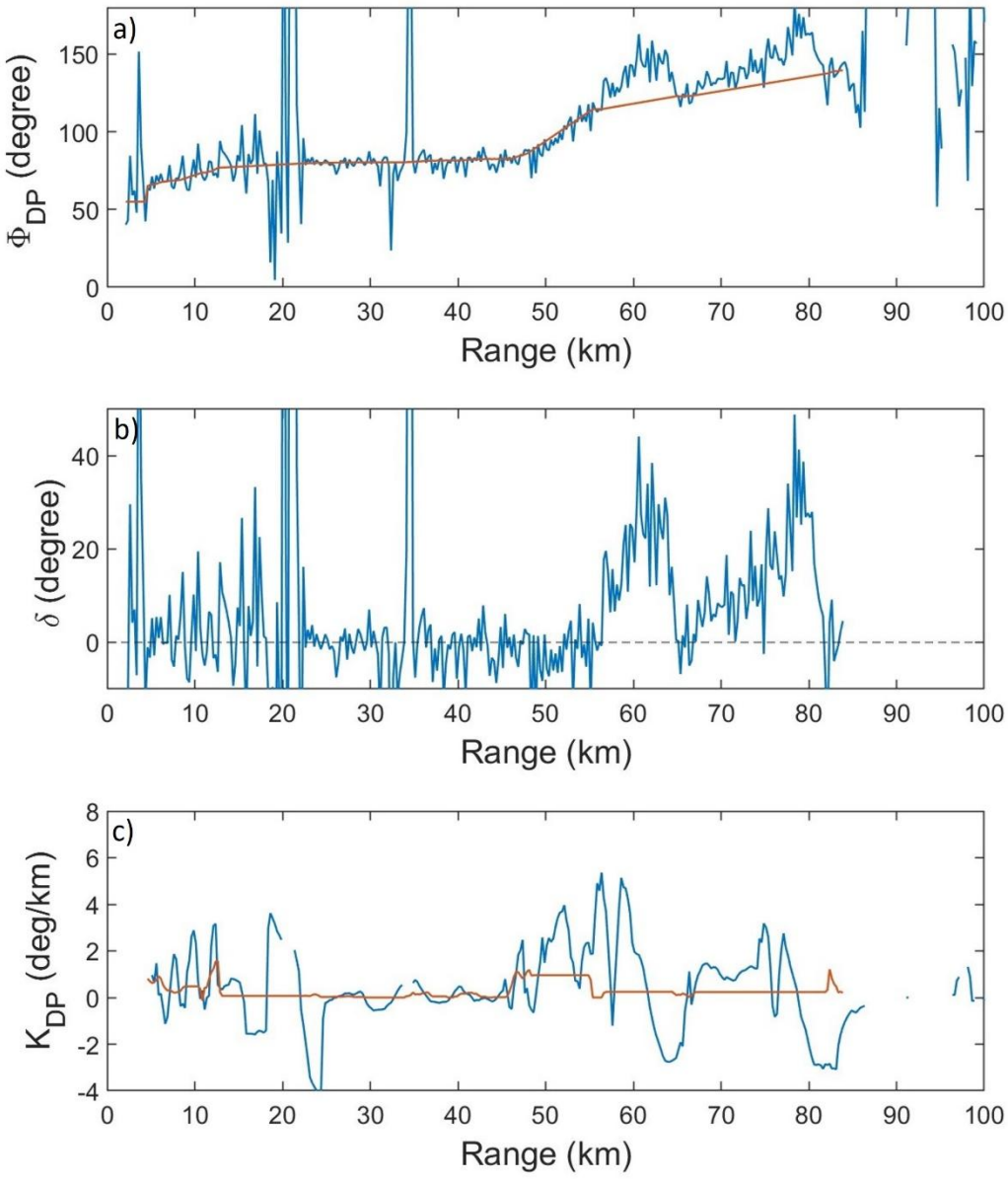


Figure 18: Estimation results for the highlighted ray plots in Figure 17: (a) measured total differential phase (blue) and estimated differential propagation phase (red), (b) estimated differential backscattering phase, (c) LSF estimated K_{DP} (blue) and LP estimated K_{DP} (red).

Figure 18 presents 1D profiles corresponding to the highlighted ray in Figure 17a-d. In Figure 18a, the estimated ϕ_{DP} (red) is plotted alongside the measured $\widehat{\Phi}_{\mathrm{DP}}$ (blue), clearly revealing the bumps in $\widehat{\Phi}_{\mathrm{DP}}$ around 60 km and 78 km, which are attributed to the δ component. The difference between these two curves represents the estimated δ, shown in Figure 18b. Notably, δ reaches peak values near 50° at the approximate locations of both hail regions.

The two K_{DP} estimation methods are compared in Figure 18c. The LSF estimation produces four distinct peaks between 47 km and 60 km, which are likely artifacts caused by δ and measurement errors. The last three peaks exhibit K_{DP} values approaching 6° km^{-1}, with negative estimates appearing between them. In contrast, the LP estimation captures an initial $\widehat{K}_{\mathrm{DP}}$ increase near 47 km but with a lower magnitude. Unlike the LSF method, the LP estimate remains relatively stable and low before gradually decreasing near 55 km, coinciding with the onset of the backscattering phase regime. Additionally, the LP method does not exhibit the sharp variations seen in the LSF estimates near the second high-reflectivity region (65–85 km), likely due to the absence of Rayleigh scattering regimes in that range.

A localized area of enhanced $\widehat{K}_{\mathrm{DP}}$ within the forward flank of a supercell, commonly referred to as the 'KDP foot,' is examined in Figure 19. This figure provides a zoomed-in view of the primary supercell responsible for producing 7.6 cm (3") hail in Amber, Oklahoma, with the 'KDP foot' outlined in purple. In Figure 19d, the LSF $\widehat{K}_{\mathrm{DP}}$ estimates show elevated values, particularly along the north-northwestern edge of the supercell, where multiple gates exceed 6° km^{-1}. In contrast, the LP estimation (Figure 19c) significantly reduces $\widehat{K}_{\mathrm{DP}}$ values throughout the supercell, particularly in the 'KDP foot' region. By limiting calculations to Rayleigh scattering regimes, the LP method reduces the influence of δ within the range derivative, a major source of error in the operational LSF approach. Despite this reduction, the LP method still captures a $\widehat{K}_{\mathrm{DP}}$

maximum in the same location as in the LSF estimate, suggesting enhanced liquid water content in a portion of the 'KDP foot'. However, the magnitude of this peak is notably lower (~3° km^{-1}), and high values do not dominate the majority of gates in the region.

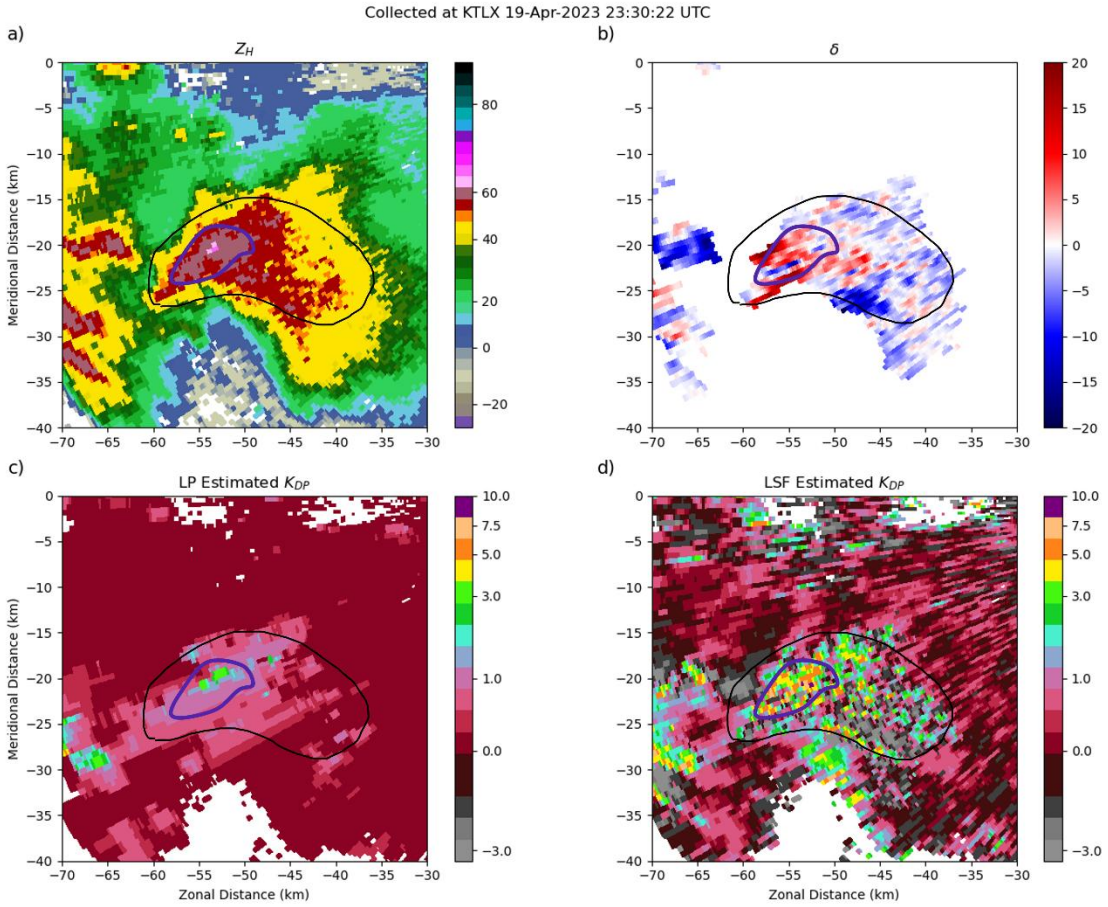


Figure 19: Illustrates primary supercell responsible for reported 3" hail in Amber, Oklahoma corresponding with scans depicted in Figure 15 and Figure 16. (a) reflectivity factor (Z_H), (b) estimated differential backscattering phase δ, (c) LP estimated K_{DP}, and (d) LSF estimated K_{DP}. The black outline is used to emphasize the area of enhanced K_{DP} seen in the LSF processing. The region of the significantly enhanced values, which is commonly referred to as 'KDP foot,' is denoted by the region within the purple line.

Figure 19b shows the estimated δ component, revealing enhanced positive δ values along the northwestern and southwestern peripheries of the Z_H maximum. Within the vicinity of the Z_H peak, δ exhibits both positive and negative values, likely due to non-Rayleigh scattering

resonance effects (illustrated in Figure 4d and Figure 5d). Additionally, a prominent negative δ signature appears along the southern edge of the supercell, which aligns with negative $\widehat{K}_{\mathrm{DP}}$ values in the LSF results (Figure 19d). This pattern likely stems from a $\widehat{\Phi}_{\mathrm{DP}}$ drop on the backside of a bump, momentarily causing the estimated ϕ_{DP} to exceed the measured $\widehat{\Phi}_{\mathrm{DP}}$—a phenomenon also visible in the 1D plot of Figure 18a between 81 and 85 km. Finally, elevated δ values south of the storm (outside the outlined region) are likely influenced by low SNR and could be filtered out to improve detection accuracy.

Since K_{DP} is theoretically defined as half the range derivative of the differential propagation phase, its estimation should be restricted to Rayleigh scattering regimes where the differential backscattering phase is negligible. Applying this restriction, as done with the LP K_{DP} estimator, results in a substantial reduction in estimated values compared to the LSF estimator. Consequently, the 'KDP foot'—an area of enhanced K_{DP} within the forward flank of the supercell—disappears. This suggests that the elevated $\widehat{K}_{\mathrm{DP}}$ values observed in LSF results arise from taking the range derivative of both ϕ_{DP} and δ, rather than isolating the propagation phase component for which K_{DP} is formally defined. Thus, the so-called 'KDP foot' appears to be an artifact of conventional operational K_{DP} estimation methodologies. Given that this feature does not truly represent K_{DP}, we propose renaming it as the "δ artifact."

Tornadoes can loft debris into the atmosphere that is comparable in size to or larger than the wavelength (~10 cm) of S-band radar, leading to returns from non-Rayleigh scattering regimes. As a result, tornado debris signatures (TDS) are expected to exhibit notable δ signals. To investigate this, we analyze two tornado cases with well-defined TDS in the radar data.

On April 19, 2023, severe thunderstorms developed along a dryline in central Oklahoma, one of which spawned a tornado in Cole, Oklahoma, producing EF3 damage and one fatality (NWS, 2023). We examine the WSR-88D KTLX 0.5° elevation scan at 0035 UTC on April 20, 2023.

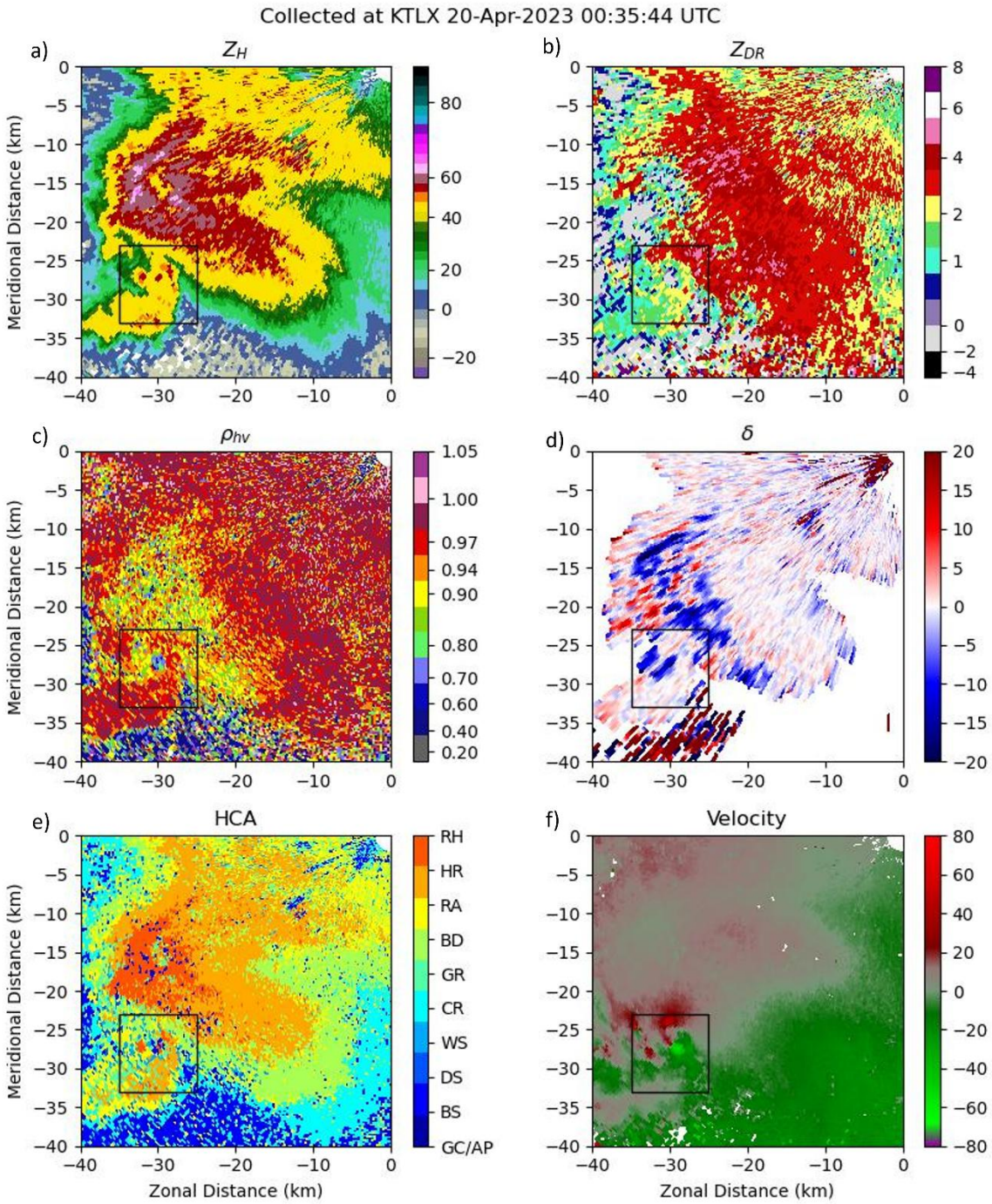


Figure 20: Illustrates low-elevation (0.5^{o}) surveillance mode data from KTLX at 0035 UTC on April 20th, 2023. (a) reflectivity factor (Z_H), (b) differential reflectivity (Z_{DR}), (c) co-polar correlation coefficient (ρ_{hv}), (d) estimated differential backscattering phase (δ), (e) hydrometeor classification, and (f) radial velocity. The black box emphasizes the region of the TDS.

A black box in each panel of Figure 20 highlights the TDS. The hook echo, indicative of the tornado's location, appears in the reflectivity field (Figure 20a). The TDS is further characterized by a negative Z_{DR} signature (Figure 20b) and a collocated region of reduced ρ_{hv} (< 0.7) (Figure 20c). As illustrated in Figure 4b and Figure 5b, resonance effects from large debris can produce highly negative Z_{DR} . Similarly, Figure 20d reveals a distinct, collocated negative δ signature, though it is not as pronounced as the TDS features in ρ_{hv} and Z_{DR}.

A second case occurred on March 24, 2023, when a violent tornado struck Rolling Fork, Mississippi, producing EF4 damage and at least 17 fatalities (NEDIS, 2023). We analyze the WSR-88D KGDX 0.5° elevation scan at 0106 UTC on March 25, 2023. Figure 21 highlights the corresponding TDS. Reflectivity values exceed 60 dBZ at the tornado's location (Figure 21a), while ρ_{hv} drops below 0.7 (Figure 21c), consistent with a strong debris signature. The Z_{DR} field (Figure 21b) shows values below 0 dB, similar to the Cole tornado case. However, unlike the Cole case, the Rolling Fork tornado exhibits a predominantly positive δ signature (Figure 21d). While a few gates near the TDS center display negative δ (~ -20°), most values range from 15° to 25°.

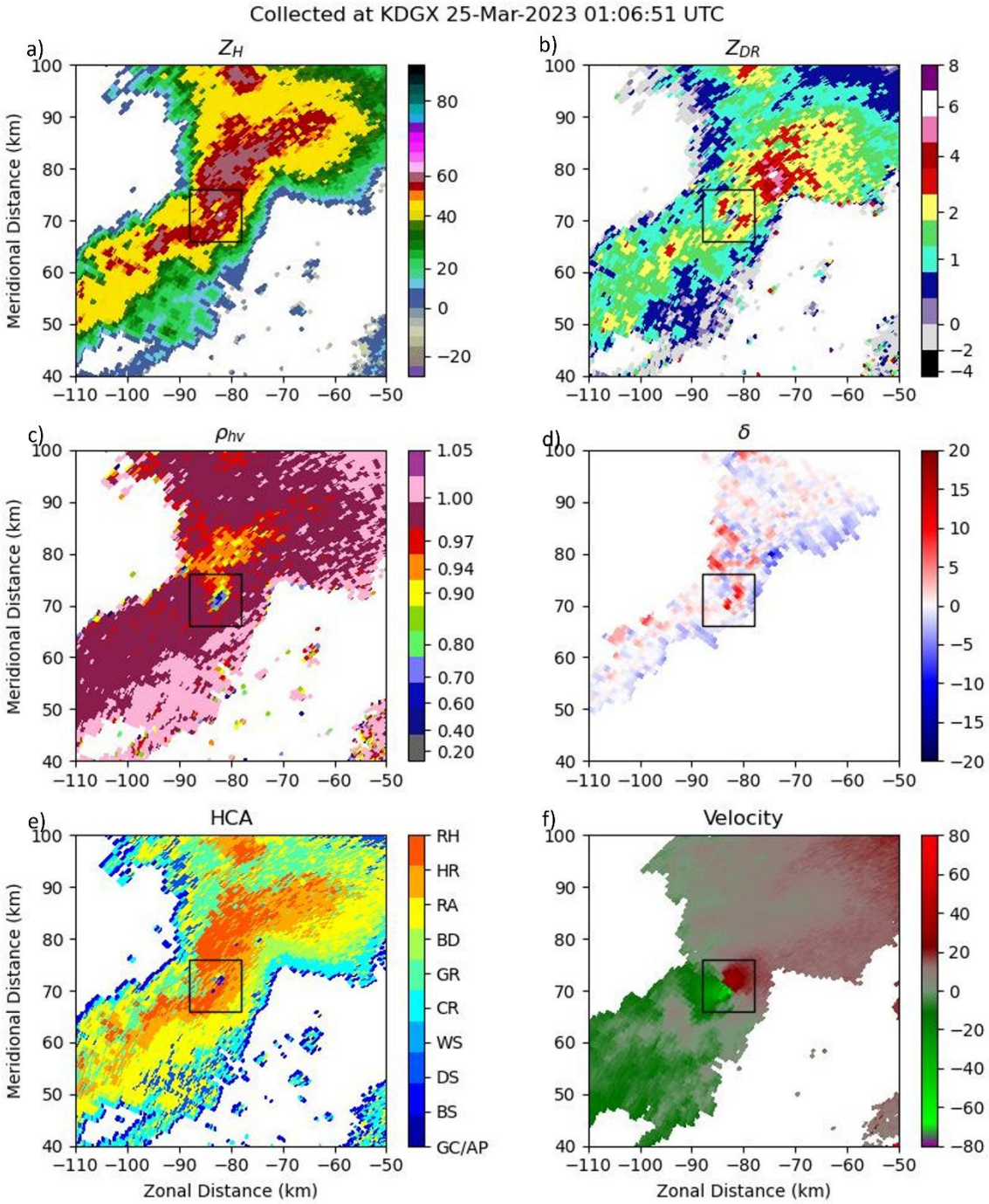


Figure 21: Illustrates low-elevation (0.5°) surveillance mode data from KDGX at 0106 UTC on March 25th, 2023. (a) reflectivity factor (Z_H), (b) differential reflectivity (Z_{DR}), (c) co-polar correlation coefficient (ρ_{hv}), (d) estimated differential backscattering phase (δ), (e) hydrometeor classification, and (f) radial velocity. The black box emphasizes the region of the TDS.

Figure 22 provides a side-by-side comparison of the TDS for both tornadoes, focusing on Z_{DR}, ρ_{hv}, and δ. The contrasting δ signatures (Figure 22c, Figure 22f) may stem from multiple factors. The Rolling Fork tornado was located farther from the radar than the Cole tornado, meaning beam broadening could have led to the simultaneous sampling of precipitation and debris. Additionally, Figure 4d and Figure 5d suggests that wet particles are less likely to produce negative δ compared to dry particles, implying that the positive δ signal may indicate a rain-wrapped tornado. This hypothesis is further supported by the higher surrounding ρ_{hv} values in the Rolling Fork case relative to the Cole case (Figure 22b, Figure 22f).

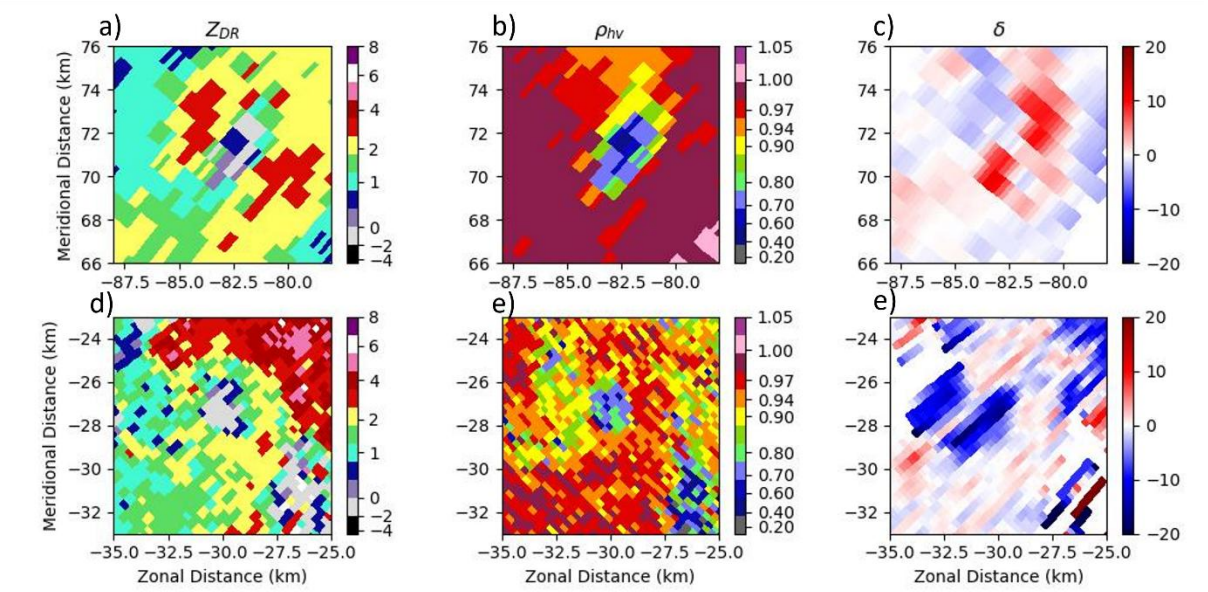


Figure 22: (a-c) display 10 by 10 km views of the Z_{DR}, ρ_{hv}, and δ signatures, respectively, for the Rolling Fork, Mississippi tornado illustrated in Figure 21 (d-f) displays the same for the Cole, Oklahoma tornado illustrated in Figure 20.

As shown in Figure 4d and Figure 5d, resonance effects in non-Rayleigh scattering regimes can yield positive, negative, or even negligible δ. While δ signatures may offer insight into scatterer location, the variability introduced by resonance effects limits their standalone use for quantitative

sizing. However, when combined with other polarimetric variables, δ could still provide valuable information regarding scatterer size distribution.

6. Summary and Conclusion

This study developed a composite approach for improving K_{DP} estimation by integrating classification and estimation techniques. Precipitation and debris scatterers (PRD) were classified into Rayleigh and non-Rayleigh scattering regimes, and the linear programming (LP) estimation method was applied exclusively to the Rayleigh regime, incorporating a nonnegativity constraint. This selective application allows for a more physically meaningful estimation of differential propagation phase while eliminating the influence of the differential backscattering phase, a known source of error in the least squares fitting (LSF) method currently used in operational settings. The classification-based LP approach thus yields more realistic K_{DP} estimates and avoids the unphysical values often introduced by the LSF method. Furthermore, by taking the difference between the observed total differential phase ($\widehat{\Phi}_{DP}$) and the estimated differential propagation phase (ϕ_{DP}), we obtained an estimate of backscatter differential phase (δ), which appears both reasonable and informative.

The analysis of non-Rayleigh scattering regimes (e.g., hail and tornado debris) revealed notable δ signatures. However, due to resonance effects at larger sizes beyond the Rayleigh scattering regime, δ does not exhibit a monotonic relationship with increasing reflectivity (Z_H). In the hail case analyzed, positive δ values were observed along the periphery of the primary hail core, while the highest Z_H regions lacked a significant backscatter signature. This suggests that resonance effects disrupt the expected correlation between hail size and δ. Similar behavior was observed in tornado debris signatures. The EF4 tornado in Rolling Fork, Mississippi (March 24, 2023) produced a well-defined tornado debris signature (TDS) with a strong positive δ collocated with

the TDS. In contrast, the EF3 tornado in Cole, Oklahoma (April 19, 2023), which also exhibited a well-defined TDS, was associated with a negative δ signature. These findings highlight the complexity of interpreting δ for debris and hail identification, as resonance effects introduce variability that complicates its direct use for scatterer sizing. While δ remains useful for identifying the presence of hail or tornado debris, caution must be exercised when inferring scatterer size due to these complicating factors.

Since K_{DP} is formally defined as half the range derivative of differential propagation phase, its estimation should be strictly confined to the Rayleigh scattering regime to avoid contamination from differential backscattering phase (δ). A comparison of the classification-based LP-derived K_{DP} with the traditional LSF-derived KDP revealed several important insights. The classification-based LP method not only eliminates unphysical negative values, but it also significantly reduces overestimated magnitudes. While the LSF method often produces $\widehat{K}_{DP}$ values exceeding $6° \, km^{-1}$ in regions of high Z_H, the LP method yields maximum values of approximately $3° \, km^{-1}$. This discrepancy is particularly evident in the leading side of supercells (relative to the radar), where the LSF method produces an exaggerated 'KDP foot' signature. Since these inflated estimates disappear when δ is properly accounted for, we propose renaming this feature from 'KDP foot' to 'δ artifact' to more accurately reflect its origin. While the LSF method retains operational utility—especially when carefully interpreted—the growing uncertainty in K_{DP} estimation as scatterer size increases beyond the Rayleigh regime underscores the need for improved methodologies.

Several potential sources of error remain unaddressed in this study. These include the use of linear interpolation across non-Rayleigh scattering regimes, which may introduce estimation errors, the presence of clutter, which can bias phase measurements, and Non-uniform beam filling (NBF), which may further complicate accurate estimation, particularly near the melting layer. Also,

though rare, Propagation cross-polarization coupling may introduce systematic bias in δ when scatterers are slantwise-oriented. Despite these challenges, our primary goal was to develop a method that produces more realistic K_{DP} estimates than those currently used operationally. This study demonstrates both the feasibility and the necessity of improving K_{DP} estimation while leveraging δ for enhanced precipitation estimation and severe weather detection. Future research will focus on expanding the LP estimator's validation across a broader range of cases, conducting comprehensive error analyses, and refining the methodology for potential operational implementation.

References

Aldana, M., S. Pulkkinen, A. von Lerber, M. R. Kumjian, and D. Moisseev, 2025: Benchmarking K_{DP} in rainfall: a quantitative assessment of estimation algorithms using C-band weather radar observations. *Atmospheric Measurement Techniques*, **18**, 793–816, https://doi.org/10.5194/amt-18-793-2025.

Amitai, E., 2000: Systematic Variation of Observed Radar Reflectivity-Rainfall Rate Relations in the Tropics. *Journal of Applied Meteorology*, 39 (12), 2198–2208, doi: 10.1175/1520-0450(2001)040⟨2198:svoorr⟩2.0.co;2.

Attisani, A., C. C, and P. A, 1974: Effects Of Non-Spherical Hydrometeors On E.M. Propagation Through Atmospheric Precipitation. *J. Rech. Atmosph.*, **8**, 137–145.

AWS, 2023: AWS S3 Explorer NOAA NEXRAD Level II. Accessed 21 May 2023, https://s3.amazonaws.com/noaa-nexrad-level2/index.html

Aydin, K. & Y. Zhao, 1990: A differential reflectivity radar hail indicator. Journal of Applied Meteorology, 29(1), 53–57.

Aydin, K., V. N. Bringi, and L. Liu, 1995: Rain-Rate Estimation in the Presence of Hail Using S-Band Specific Differential Phase and Other Radar Parameters. *J. Appl. Meteor. Climatol.*, **34**, 404–410, https://doi.org/10.1175/1520-0450-34.2.404.

Balakrishnan, N., and D. S. Zrnić, 1990: Use of polarization to characterize precipitation and discriminate large hail. *J. Atmos. Sci*, **47**, 1525–1540.

Bluestein, H. B., & R. M. Wakimoto, 2003: Mobile Doppler Radar Observations of Tornadoes and Supercells: A Review of the First Decade. *Monthly Weather Review*, 131(2), 293–308.

Boerner, W. M., Holt, J. M., Livingstone, C. E., and Morrison, R. J., 1981: Interactions of electromagnetic waves with complex objects and polarization phenomenology. *Proceedings of the IEEE,* 69(10), 1259–1305.

Brandes, E. A., G. Zhang, and J. Vivekanandan, 2002: Experiments in rainfall estimation with a polarimetric radar in a subtropical environment. *J. Appl. Meteor. Climatol.*, **41**, 674–685, https://doi.org/10.1175/1520-0450(2002)041<0674:EIREWA>2.0.CO;2.

Bringi, V. N., and V. Chandrasekar, 2001: *Polarimetric Doppler Weather Radar: Principles and Applications*. Cambridge University Press, 636 pp.

Cao, Q., G. Zhang, E. Brandes, T. Schuur, A. Ryzhkov, and K. Ikeda, 2008: Analysis of video disdrometer and polarimetric radar data to characterize rain microphysics in Oklahoma. *Journal of Applied Meteorology and Climatology*, **47**, 2238–2255, doi:10.1175/2008jamc1732.1.

Chu, T. S., 1974: Rain-Induced Cross-Polarization at Centimeter and Millimeter Wavelengths. *Bell System Technical Journal*, **53**, 1557–1579, https://doi.org/10.1002/j.1538-7305.1974.tb02804.x.

Danielsen, E. F., R. Bleck, & D. A. Morris, 1972: Hail growth by stochastic collection in a cumulus model. *Journal of the Atmospheric Sciences*, *29*(1), 135–155. doi:10.1175/1520-0469(1972)029<0135:hgbsci>2.0.co;2

Doviak, R. J., and Zrníc Dúsn S., 1984, 1993: *Doppler radar and weather observations*. Academic Press, San Diego, CA.

Doviak, R. J., V. Bringi, A. Ryzhkov, A. Zahrai, and D. Zrnic, 2000: Considerations for Polarimetric Upgrades to Operational WSR-88D Radars. Journal of Atmospheric and Oceanic Technology, 17 (3), 257–278, doi:10.1175/1520-0426(2000)017⟨0257:cfputo⟩ 2.0.co;2.

Doviak, R., & Zrnić, D. S., 1993: *Doppler Radar and Weather Observations* Academic Press. pp. 562.

Fabry, F., 2015: Radar Meteorology: Principles and Practice. Cambridge University Press, pp. 256.

Geng, F., and L. Liu, 2023: Study on the Backscatter Differential Phase Characteristics of X-Band Dual-Polarization Radar and its Processing Methods. *Remote Sensing*, **15**, 1334, https://doi.org/10.3390/rs15051334.

Giangrande, S. E., and A. V. Ryzhkov, 2008: Estimation of rainfall based on the results of polarimetric echo classification. *J. Appl. Meteor. Climatol.*, **47**, 2445–2462, https://doi.org/10.1175/2008JAMC1753.1.

Giangrande, S. E., R. McGraw, and L. Lei, 2013: An application of linear programming to polarimetric radar differential phase processing. *J. Atmos. Oceanic Technol.*, **30**, 1716–1729, https://doi.org/10.1175/JTECH-D-12-00147.1.

Grams, H. M., 2019: Dual polarization quantitative precipitation estimation on the WSR-88D: Current status and future plans. *AMS supported meetings*. AMS. https://ams.confex.com/ams/2019Annual/webprogram/Paper352300.html.

Houser, J. L., H. B. Bluestein, and J. C. Snyder, 2016: A Finescale Radar Examination of the Tornadic Debris Signature and Weak-Echo Reflectivity Band Associated with a Large, Violent Tornado. Monthly Weather Review, 144 (11), 4101–4130, doi:10. 1175/mwr-d-15-0408.1.

Huang, H., G. Zhang, K. Zhao, and S. Giangrande, 2016: A hybrid method to estimate specific differential phase and rainfall with linear programming and physics constraints. *IEEE Trans. Geosci. Remote Sens.***55**, 1–16, https://doi.org/10.1109/TGRS.2016.2596295.

Huang, H., K. Zhao, H. Chen, G. Chen, D. Hu, Y. Zhang, and Z. Yang, 2021: Improving Time-Efficiency of Variational Specific Differential Phase Estimation. *IEEE Transactions on Geoscience and Remote Sensing*, **59**, 5642–5664, https://doi.org/10.1109/TGRS.2020.3020914.

Hubbert, J., and V. N. Bringi, 1995: An Iterative Filtering Technique for the Analysis of Copolar Differential Phase and Dual-Frequency Radar Measurements. Journal of Atmospheric and Oceanic Technology, 12 (3), 643–648, doi:10.1175/1520-0426(1995) 012⟨0643:aiftft⟩2.0.co;2.

Hubbert, J. C., Dixon, M., Ellis, S. M., & G. Meymaris, 2009: Weather radar ground clutter. part I: Identification, modeling, and simulation. *Journal of Atmospheric and Oceanic Technology*, *26*(7), 1165–1180. doi:10.1175/2009jtecha1159.1

Huynen, J. R., 1970: Phenomenological theory of radar targets. Eindhoven University of Technology, Eindhoven, The Netherlands.

Istok, M. J., & Doviak, R. J. (1986). Spectrum Width Estimation and Its Applications in Radar Meteorology. Journal of Atmospheric and Oceanic Technology, 3(4), 514–526.

Jung, Y., G. Zhang, and M. Xue, 2008: Assimilation of simulated polarimetric radar data for a convective storm using the ensemble Kalman filter. Part I: Observation operators for reflectivity and polarimetric variables. *Mon. Wea. Rev.*, **136**, 2228–2245, https://doi.org/10.1175/2007MWR2083.1.

Kennaugh, E. M., 1952: Polarization properties of radar reflections. Ohio State University, Antenna Laboratory Report, No. 389.

Kessler, E. (1969). On the distribution and continuity of water substance in atmospheric circulations. *On the Distribution and Continuity of Water Substance in Atmospheric Circulations*, 1–84. doi:10.1007/978-1-935704-36-2_1

Kim, T.-J., H.-H. Kwon, and K. B. Kim, 2021: Calibration of the reflectivity-rainfall rate (Z-R) relationship using long-term radar reflectivity factor over the entire South Korea region in a Bayesian perspective. *Journal of Hydrology*, **593**, https://doi.org/10.1016/j.jhydrol.2020.125790.

Kumjian, M. R., and A. V. Ryzhkov, 2008: Polarimetric signatures in supercell thunderstorms. *J. Appl. Meteor. Climatol.*, **47**, 1940–1961, https://doi.org/10.1175/2007JAMC1874.1.wang

Kumjian, M., 2013: Principles and applications of dual-polarization weather radar. Part II: Warm- and cold-season applications. *J. Operational Meteor.*, **1**, 243–264, https://doi.org/10.15191/nwajom.2013.0120.

Kumjian, M., 2013: Principles and applications of dual-polarization weather radar. Part I: Description of the polarimetric radar variables. *J. Operational Meteor.*, **1**, 226–242, https://doi.org/10.15191/nwajom.2013.0119.

Li, X., & G. Zhang, 2022: Contributions to Doppler Spectrum Width from Hydrometeor Dynamics and Microphysics. Journal of Applied Meteorology and Climatology, 61(1), 55–68.

Maesaka, T., K. Iwanami, and M. Maki, 2012: Non-negative KDP Estimation by Monotone Increasing PHIDP Assumption below Melting Layer. The Seventh European Conference on Radar in Meteorology and Hydrology, European Conference on Radar in Meteorology and Hydrology, Toulouse, France.

Mancini, A., J. L. Salazar, R. M. Lebr´on, and B. L. Cheong, 2018: A Novel Instrument for Real-Time Measurement of Attenuation of Weather Radar Radome Including Its Outer Surface. Part I: The Concept. *Journal of Atmospheric and Oceanic Technology*, **35** (5), 953–973, doi:10.1175/jtech-d-17-0083.1.

Marshall, J. S., and W. M. K. Palmer, 1948: THE DISTRIBUTION OF RAINDROPS WITH SIZE. *Journal of Meteorology*, **5** (4), 165–166, doi:10.1175/1520-0469(1948) 005⟨0165:tdorws⟩2.0.co;2.

Matrosov, S. Y., R. Cifelli, P. C. Kennedy, S. W. Nesbitt, S. A. Rutledge, V. N. Bringi, and B. E. Martner, 2006: A Comparative Study of Rainfall Retrievals Based on Specific Differential Phase Shifts at X- and S-Band Radar Frequencies. *Journal of Atmospheric and Oceanic Technology*, **23** (7), 952–963, doi:10.1175/jtech1887.1.

McCormick, G. C., and A. Hendry, 1975: Principles for the radar determination of the polarization properties of precipitation. *Radio Science*, **10**, 421–434, https://doi.org/10.1029/RS010i004p00421.

Melnikov, V. M., M. J. Istok, and J. K. Westbrook, 2015: Asymmetric Radar Echo Patterns from Insects. *Journal of Atmospheric and Oceanic Technology*, 32 (4), 659674, doi:10.1175/jtech-d-13-00247.1.

Mie, G., 1908: Beiträge zur Optik trüber Medien, speziell kolloidaler Metallösungen. *Annalen der Physik*, **330**, 377–445, https://doi.org/10.1002/andp.19083300302.

Mishler, R., G. Zhang, and V. N. Mahale, 2024: Improving Estimation of Specific Differential Phase and Assessing Differential Backscattering Phase. *J. Appl. Meteor. Climatol.*, **63**, 803–819, https://doi.org/10.1175/JAMC-D-23-0204.1.

NESDIS, 2023: Violent Storms Tear Through the South. Accessed 09 October 2023, https://www.nesdis.noaa.gov/news/violent-storms-tear-through-the-south#:~:text=The%20first%20tornadoes%20touched%20down,mph%2C%20that%20injured%20five%20people

NWS, 2023: Severe Weather and Tornado Outbreak of April 19, 2023. Accessed 09 October 2023, https://www.weather.gov/oun/events-20230419#:~:text=The%20tornado%20that%20occurred%20in,were%20given%20EF%2D0%20ratings

Oguchi, T., 1977: Scattering properties of Pruppacher-and-Pitter form raindrops and cross polarization due to rain: Calculations at 11, 13, 19.3, and 34.8 GHz. *Radio Science*, **12**, 41–51, https://doi.org/10.1029/RS012i001p00041.

Otto, T., and H. W. J. Russchenberg, 2011: Estimation of specific differential phase and differential backscatter phase from polarimetric weather radar measurements of rain. *IEEE Geosci. Remote Sens. Lett.*, **8**, 988–992, https://doi.org/10.1109/LGRS.2011.2145354.

Picca, J., and A. Ryzhkov, 2012: A Dual-Wavelength Polarimetric Analysis of the 16 May 2010 Oklahoma City Extreme Hailstorm. *Monthly Weather Review*, **140**, 1385–1403, https://doi.org/10.1175/MWR-D-11-00112.1.

Ralph-Hampton, J.M., 2022: Studying the uncertainty in Specific Differential Phase (K_{DP}) from weather radar measurements. Dissertation, School of Earth and Environment, The University of Leeds, 152 pp., https://etheses.whiterose.ac.uk/31666/1/ralph-hampton_joshua_thesis.pdf

Reimel, K. J., and M. Kumjian, 2021: Evaluation of KDP Estimation Algorithm Performance in Rain Using a Known-Truth Framework. *Journal of Atmospheric and Oceanic Technology*, **38**, 587–605, https://doi.org/10.1175/JTECH-D-20-0060.1.

Romine, G. S., D. W. Burgess, and R. B. Wilhelmson, 2008: A dual-polarization-radar-based assessment of the 8 May 2003 Oklahoma City area tornadic supercell. *Mon. Wea. Rev.*, **136**, 2849–2870, https://doi.org/10.1175/2008MWR2330.1.

Ryzhkov, A. V. 2007. The impact of beam broadening on the quality of radar polarimetric data. *Journal of Atmospheric and Oceanic Technology*, 24, 729–744.

Ryzhkov, and D. S. Zrnić, 1998: Beamwidth effects on the differential phase measurements of rain. *J. Atmos. Oceanic Technol.*, **15**, 624–634, https://doi.org/10.1175/1520-0426(1998)015<0624:BEOTDP>2.0.CO;2.

Ryzhkov, A. V., and D. S. Zrnic, 2019: Radar Polarimetry for Weather Observations. *Springer Atmospheric Sciences*, 486 pp., doi:10.1007/978-3-030-05093-1.

Ryzhkov, A. V., S. E. Giangrande, and T. J. Schuur, 2005a: Rainfall estimation with a polarimetric prototype of WSR-88D. *J. Appl. Meteor.*, **44**, 502–515, https://doi.org/10.1175/JAM2213.1.

Ryzhkov, A. V., T. J. Schuur, D. W. Burgess, and D. S. Zrnić, 2005b: Polarimetric tornado detection. *J. Appl. Meteor. Climatol.*, **44**, 557–570, https://doi.org/10.1175/JAM2235.1.

Ryzhkov, A., M. Pinsky, A. Pokrovsky, and A. Khain, 2011: Polarimetric Radar Observation Operator for a Cloud Model with Spectral Microphysics. *Journal of Applied Meteorology and Climatology*, *50* (4), 873–894, doi:10.1175/2010jamc2363.1.

Sachidananda, M., and D. S. Zrnić, 1989: Efficient Processing of Alternately Polarized Radar Signals. *Journal of Atmospheric and Oceanic Technology*, **6**, 173–181, doi: https://doi.org/10.1175/1520-0426(1989)006<0173:EPOAPR>2.0.CO;2

Schneebeli, M., and A. Berne, 2012: An Extended Kalman Filter Framework for Polarimetric X-Band Weather Radar Data Processing. *Journal of Atmospheric and Oceanic Technology*, **29**, 711–730, https://doi.org/10.1175/JTECH-D-10-05053.1.

Schneebeli, M., J. Sakuragi, T. Biscaro, C. F. Angelis, I. Carvalho da Costa, C. Morales, L. Baldini, and L. A. T. Machado, 2012: Polarimetric X-band weather radar measurements in the tropics: radome and rain attenuation correction. *Atmospheric Measurement Techniques*, **5** (9), 2183–2199, doi:10.5194/amt-5-2183-2012.

Seliga, T. A., and V. N. Bringi, 1976: Potential use of radar differential reflectivity measurements at orthogonal polarizations for measuring precipitation. *Journal of Applied Meteorology*, **15**, 69–76, doi:10.1175/1520-0450(1976)015<0069:puordr>2.0.co;2.

Seliga, T. A., V. N. Bringi, , & H. H. Al-khatib, 1979: Differential reflectivity measurements in rain: First experiments. *IEEE Transactions on Geoscience Electronics*, *17*(4), 240–244. doi:10.1109/tge.1979.294652

Seliga, T. A., and V. N. Bringi, 1978: Differential reflectivity and differential phase shift: Applications in radar meteorology. *Radio Sci.*, **13**, 271–275, https://doi.org/10.1029/RS013i002p00271.

Smith, J. A., and W. F. Krajewski, 1993: A modeling study of rainfall rate-reflectivity relationships. *Water Resources Research*, **29** (8), 2505–2514, doi:10.1029/93wr00962.

Smith, P. L., C. G. Myers, & H. D. Orville, 1975: Radar reflectivity factor calculations in numerical cloud models using bulk parameterization of precipitation. *Journal of Applied Meteorology*, *14*(6), 1156–1165. doi:10.1175/1520-0450(1975)014<1156:rrfcin>2.0.co;2

SPC, 2023: 20230419's Storm Reports (20230419 1200 UTC - 20230420 1159 UTC). Accessed 16 October 2023, https://www.spc.noaa.gov/exper/archive/event.php?date=20230419

Stepanian, P. M., K. G. Horton, V. M. Melnikov, D. S. Zrnić, and S. A. Gauthreaux Jr., 2016: Dual-polarization radar products for biological applications. *Ecosphere*, **7**, e01539, https://doi.org/10.1002/ecs2.1539.

Stout, G. E., and E. A. Mueller, 1968: Survey of Relationships Between Rainfall Rate and Radar Reflectivity in the Measurement of Precipitation. *Journal of Applied Meteorology*, **7**(3), 465–474, doi:10.1175/1520-0450(1968)007⟨0465:sorbrr⟩2.0.co;2.

Tokay, A., P. G. Bashor, E. Habib, and T. Kasparis, 2008: Raindrop size distribution measurements in tropical cyclones. *Monthly Weather Review*, **136**, 1669–1685, doi:10.1175/2007mwr2122.1.

Trapp, R. J., and Coauthors, 2020: Multiple-Platform and Multiple-Doppler Radar Observations of a Supercell Thunderstorm in South America during RELAMPAGO. Monthly Weather Review, 148 (8), 3225–3241, doi:10.1175/mwr-d-20-0125.1.

Trömel, S., A. V. Ryzhkov, P. Zhang, and C. Simmer, 2014: Investigations of Backscatter Differential Phase in the Melting Layer. *Journal of Applied Meteorology and Climatology*, **53**, 2344–2359, https://doi.org/10.1175/JAMC-D-14-0050.1.

Trömel, S., M. R. Kumjian, A. V. Ryzhkov, C. Simmer, and M. Diederich, 2013: Backscatter differential phase—Estimation and variability. *J. Appl. Meteor. Climatol.*, **52**, 2529–2548, https://doi.org/10.1175/JAMC-D-13-0124.1.

Ulbrich, C. W., & D. Atlas, 1984: Assessment of the contribution of differential polarization to improved rainfall measurements. *Radio Science*, *19*(1), 49–57. doi:10.1029/rs019i001p00049

Ulbrich, C. W., & L. G. Lee, 1999: Rainfall measurement error by WSR-88D radars due to variations in*Z*–*r*law parameters and the radar constant. *Journal of Atmospheric and Oceanic Technology*, *16*(8), 1017–1024. doi:10.1175/1520-0426(1999)016<1017:rmebwr>2.0.co;2

Vivekanandan, J., W. Adams, and V. Bringi, 1991: Rigorous approach to polarimetric radar modeling of hydrometeor orientation distributions. *J. Appl. Meteor.*, **30**, 1053-1063.

Vivekanandan, J., G. Zhang, and M. K. Politovich, 2001: An assessment of droplet size and liquid water content derived from dual-wavelength radar measurements to the application of aircraft icing detection. *J. Atmos. Oceanic Technol.*, **18**, 1787–1798, https://doi.org/10.1175/1520-0426(2001)018<1787:AAODSA>2.0.CO;2.

Wang, Y., and V. Chandrasekar, 2009: Algorithm for estimation of the specific differential phase. *J. Atmos. Oceanic Technol.*, **26**, 2565–2578, https://doi.org/10.1175/2009JTECHA1358.1.

Wang, Y., and V. Chandrasekar, 2010: Quantitative precipitation estimation in the CASA x-band dual-polarization radar network. *J. Atmos. Oceanic Technol.*, **27**, 1665–1676, https://doi.org/10.1175/2010JTECHA1419.1.

Waterman, P.C., 1965: Matrix formulation of electromagnetic scattering. *Proc. IEEE*, **53**, 805-812, https://doi.org/10.1109/PROC.1965.4058.

WDTD, 2024: Dual-Polarization Hail Analysis. Accessed 1 Mar 2025, https://training.weather.gov/wdtd/courses/rac/severe/dp-hail-analysis/story.html.

Westbrook, C. D., A. J. Illingworth, E. J. O'Connor, and R. J. Hogan, 2010: Doppler lidar measurements of oriented planar ice crystals falling from supercooled and glaciated layer clouds. *Quart. J. Roy. Meteor. Soc.*, **136**, 260–276, https://doi.org/10.1002/qj.528.

Willmarth, W. W., N. E. Hawk, & R. L. Harvey, 1964: Steady and unsteady motions of small particles in a boundary layer. The Physics of Fluids, 7(2), 197–208.

Wilson, M. B., and M. S. Van Den Broeke, 2021: An automated python algorithm to quantify Z_{DR} arc and K_{DP}–Z_{DR} separation signatures in supercells. *J. Atmos. Oceanic Technol.*, **38**, 371–386, https://doi.org/10.1175/JTECH-D-20-0056.1.

Zhang, G., 2016: *Weather Radar Polarimetry*. CRC Press, 304 pp.

Zhang, G., and Coauthors, 2019: Current status and future challenges of weather radar polarimetry: Bridging the gap between Radar Meteorology/hydrology/engineering and numerical weather prediction. *Advances in Atmospheric Sciences*, **36**, 571–588, doi:10.1007/s00376-019-8172-4.

Zhang, G., J. Vivekanandan, & E. Brandes, 2001: A method for estimating rain rate and drop size distribution from polarimetric radar measurements. *IEEE Transactions on Geoscience and Remote Sensing*, *39*(4), 830–841. doi:10.1109/36.917906

Zhang, G, J. Gao, and M. Du, 2021: Parameterized forward operators for simulation and assimilation of polarimetric radar data with numerical weather predictions. *Adv. Atmos. Sci.*, **38**, 737–754, https://doi.org/10.1007/s00376-021-0289-6.

Zhang, J., L. Tang, S. Cocks, P. Zhang, A. Ryzhkov , K. Howard, 2020: A dual-polarization radar synthetic QPE for Operations. *Journal of Hydrometeorology*, *21*(11), 2507–2521. doi:10.1175/jhm-d-19-0194.1

Zrnić, D. S., and A. Ryzhkov, 1996: Advantages of rain measurements using specific differential phase. *J. Atmos. Oceanic Technol.*, **13**, 454–464, https://doi.org/10.1175/1520-0426(1996)013<0454:AORMUS>2.0.CO;2.

Zrnic, D. S., N. Balakrishnan, C. L. Ziegler, V. N. Bringi, K. Aydin, and T. Matejka, 1993: Polarimetric Signatures in the Stratiform Region of a Mesoscale Convective System. *Journal of Applied Meteorology and Climatology*, **32**, 678–693, https://doi.org/10.1175/1520-0450(1993)032<0678:PSITSR>2.0.CO;2.